




Chair of Mining Engineering and Mineral Economics

Master's Thesis



Numerical CFD Simulation of Geothermal  
Heat Exchangers

Alexander Steurer, BSc

September 2021



Master's Thesis

---

## Numerical CFD Simulation of Geothermal Heat Exchangers

---

Alexander Steurer, BSc.

Matr.Nr.: m01335261



Chair of Mining Engineering and Mineral Economics

Internal Advisors:

Univ.-Prof. Dipl.-Ing. Dr.mont. Nikolaus August Sifferlinger

Dipl.-Ing. Dr.mont. Michael Prenner

External Advisor:

Dipl.-Ing. Dr. Christoph Reichl

Wien, Oktober 2021



**MONTANUNIVERSITÄT LEOBEN**  
www.unileoben.ac.at

### EIDESSTATTLICHE ERKLÄRUNG

Ich erkläre an Eides statt, dass ich diese Arbeit selbständig verfasst, andere als die angegebenen Quellen und Hilfsmittel nicht benutzt, und mich auch sonst keiner unerlaubten Hilfsmittel bedient habe.

Ich erkläre, dass ich die Richtlinien des Senats der Montanuniversität Leoben zu "Gute wissenschaftliche Praxis" gelesen, verstanden und befolgt habe.

Weiters erkläre ich, dass die elektronische und gedruckte Version der eingereichten wissenschaftlichen Abschlussarbeit formal und inhaltlich identisch sind.

Datum 26.08.2021

Unterschrift Verfasser/in  
Alexander Steurer

---

## Acknowledgements

First and foremost, I would like to thank my supervisor Dipl.-Ing. Dr. Christoph Reichl for the competent support, whenever necessary.

I would also like to thank the whole GEOFIT team for the great time at AIT. Although the final practical activities were overshadowed by the outbreak of the COVID-19 pandemic, the scientific discourse and the exchange of ideas did not stop. I also have to thank Dipl.-Ing. Dr. Michael Lauermann, who always had an open ear. I would like to particularly emphasise my friend and supporter Dipl.-Ing. Stephan Kling, whose ideas were indispensable for the progress of the whole project. Maybe we find out one day, whether entropy and chaos really rule the world. I would also like to thank Dipl.-Ing. Dr. Edith Haslinger, who led the whole men's group in a great manner.

A big thank to Dipl.-Ing. Constantin Zenz and Dipl.-Ing. Constantin Doerr as well. The friendly discourse and CFD support, whenever needed, was invaluable for the completion of this thesis.

Additionally I would also like to recognize Dipl. Ing. Dr. mont. Michael Prenner and Univ.-Prof. Dipl.-Ing. Dr. mont. Nikolaus August Sifferlinger from the University of Leoben for the support from university's side, as well as fast responses to any question I had.

Finally, my deepest appreciation goes to my whole family, for the support throughout my whole life and studies. Warm thanks also to my girlfriend Melanie. Without her strong support, I probably would not have completed my coursework by 2021.

---

## Kurzfassung

Diese Masterarbeit wurde in Zusammenarbeit mit dem österreichischen Forschungsinstitut *Austrian Institute of Technology* (AIT) im Rahmen des *GEOFIT* Projektes durchgeführt. Dieses Forschungsprojekt ist in das europäische Förderprogramm Horizon 2020 eingebettet. Ziel der vorliegenden Arbeit ist es, die Nahfeldeigenschaften von neuartigen, platzsparenden Erdwärmetauschern (Erdkörbe und Ringgrabenkollektoren) in verschiedenen Substraten zu erfassen und zu dokumentieren. Ergänzend zu den experimentellen Versuchsaufbauten sollen Simulationen ein reproduzierbares physikalisches Abbild schaffen und Daten für ein Dimensionierungstool bereitstellen. Die Daten aus der Nahfeldsimulation sind zudem ein wichtiger Input für weitergehende Betrachtungen in Fernfeldsimulationen. Diese werden vom europäischen Partnerinstitut EURECAT durchgeführt.

Als Grundlage und Vergleichsbasis für diverse Simulationsreihen dient ein experimenteller Versuchsaufbau unter kontrollierten Bedingungen innerhalb einer Klimakammer am AIT. Die räumliche und zeitliche Auflösung des Temperaturfeldes wird von faseroptischen Sensoren und PT1000 Sensoren erfasst und bereitgestellt. Da sich eine hinreichend genaue modellhafte 3D-Darstellung des Versuchsaufbaues als sehr ressourcenaufwändig herausstellte, wurden alternativ sowohl ein vereinfachtes 2D Zylindermodell entwickelt, als auch ein 1D Stabmodell. Mithilfe des 1D Stabmodells konnte zudem die Richtigkeit des Berechnungsalgorithmus gezeigt werden. Tests mit verschiedenen Zeitschritten resultierten in der Erkenntnis, dass durch optimale Wahl der Simulationseinstellungen signifikante Rechenleistung gespart werden kann.

Aus ersten Vergleichen von Experiment und Simulation, durchgeführt mit trockenem Sand als Substrat, gehen deutliche Abweichungen der Temperaturfelder hervor. Weitere Berechnungen mit temperaturabhängigen Materialkennwerten aus Laboruntersuchungen konnten Fehlerursachen systematisch ausschließen. Mithilfe der Simulationsergebnisse konnte auch ein Verständnis für die verschiedenen Stellschrauben des Temperaturfeldes, das durch die partielle Differentialgleichung (DGL) der Wärmeleitung beschrieben wird, gewonnen werden. Wichtig fürs Verständnis ist dabei die Erkenntnis, dass die Wärmeleitfähigkeit  $\lambda$  Information über den partikulären Teil der DGL liefert, während der Faktor  $\rho \cdot c_p$  Information für den flüchtigen Teil der DGL liefert.

Des Weiteren wurden dem europäischen Forschungspartner EURECAT Temperaturverteilungen und Wärmeflüsse auf einem Zylindermantel bereitgestellt, um weiterer globale Feldsimulationen durchführen zu können.

Eine abschließende Parameterstudie mit verschiedenen Steigungen und Durchmessern der Heizhelix ermöglicht erste Abschätzungen von Geometrieänderungen auf die auftretenden Wärmeflüsse. Dies soll die Grundlage für weiteren internationalen wissenschaftlichen Diskurs darstellen und die Weiterentwicklung von oberflächennahen Erdwärmetauschern als Teil von Wärmepumpensystemen fördern.

---

## Abstract

This master thesis was carried out in cooperation with the Austrian Institute of Technology (AIT) as part of the GEOFIT project. This research project is embedded in the European funding programme Horizon 2020. The aim of the present work is to record and document the near-field properties of novel, space-saving geothermal heat exchangers (earth baskets and trench collectors) in different soil types. In addition to the experimental test set-ups, simulations are used to create a reproducible physical image and provide data for a dimensioning tool. The data from the near-field simulation are also an important input for further considerations in far-field simulations. These are carried out by the European partner institute EURECAT.

An experimental test set-up under controlled conditions in a climate chamber at the AIT serves as basis and comparison for various simulation series. The spatial and temporal resolution of the temperature field is recorded and provided by fibre-optic sensors and PT1000 sensors. Since a sufficiently accurate 3D model representation of the experimental setup turned out to be very resource-intensive, both a simplified 2D cylinder model and a 1D rod model were developed as alternatives. In addition, the correctness of the calculation algorithm could be proven by the 1D rod model. Tests with different time steps resulted in significant reduction of the calculation effort by choosing optimal simulation parameters.

The first series of experiments, carried out with dry sand, showed clear differences in the temperature field compared to the simulation. Various simulation series with temperature-dependent material parameters from laboratory tests were able to systematically exclude error causes. It was also possible to gain an understanding of the various adjusting screws of the temperature field, which is mathematically described by the partial DGL of heat conduction. The thermal properties of the soil are unambiguously determined by the thermal diffusivity  $a$ . It is important to realise, that the temperatures reached in the steady state of the system depend exclusively on the value of the thermal conductivity  $\lambda$ , while the transient solution depends on the combination of the factor  $\rho \cdot c_p$ .

Furthermore, the European research partner EURECAT was provided with temperature distributions and heat fluxes on a cylinder jacket in order to carry out further global field simulations.

A final parameter study using different pitches and diameters of the heating helix gives insights into first tendencies regarding the heat flux. This should provide a base line for further international scientific discourse and promote further development of shallow geothermal heat exchangers as part of heat pump systems.

---

## Table of contents

List of Figures .....	VIII
List of Tables.....	IX
List of abbreviations & symbols .....	X
1 Introduction .....	1
2 GEOFIT Objectives.....	3
3 State of the Art .....	4
3.1 Ground Source Heat Exchangers .....	4
3.2 Low-Depth Spiral Heat Exchanger Types.....	6
3.3 Influence of system parameters:.....	7
3.3.1 Ground Temperature .....	8
3.3.2 Ground properties.....	8
3.3.3 Geometrical properties .....	8
4 Theory of Heat Conduction.....	9
4.1 Classification of systems .....	9
4.2 First Law of Thermodynamics .....	10
4.3 Second Law of Thermodynamics.....	11
4.4 Principles of Heat Transfer.....	11
4.5 Principle of Heat Conduction .....	12
4.6 Stationary/Transient Heat Conduction .....	12
4.7 The Law of Fourier.....	13
4.8 Differential heat conduction equation .....	14
4.8.1 Definition of the general equation.....	14
4.9 Simplifications and Boundary Conditions (BC) .....	19
4.9.1 Simplifications.....	19
4.9.2 Boundary Conditions.....	19
5 Experimental site.....	22
5.1 Testing strategy .....	22
5.2 Experimental setup .....	22
6 Validation of the numerical ANSYS Fluent Code .....	25
6.1 1-D heat equation .....	25

---

6.2	Definition of the heat-source .....	26
6.3	Comparison of a numeric solution and the <i>ANSYS® Fluent</i> algorithm: .....	27
7	Geometry & Mesh .....	29
7.1	Geometry .....	29
7.2	Mesh .....	30
7.3	Implementation of the Sensorpoints .....	32
7.4	Boundary Conditions .....	34
7.5	Soil characterization .....	34
7.6	Simplification into 2D space .....	35
8	Comparison of experiment and simulation .....	36
8.1	Experiment .....	36
8.2	Simulation vs. Experiment .....	37
9	Parameter Variation .....	38
9.1	Time-Step Variation .....	38
9.2	Local mesh-refinement .....	40
9.3	Variation of $a$ in 2D .....	41
9.4	Variation of $a$ in 1D .....	43
9.5	Variation of the density $\rho$ .....	44
9.6	Variation of the heat transfer coefficient $\alpha$ .....	45
9.7	Variation of the Power input .....	46
9.7.1	2D cylinder model .....	46
9.7.2	3D helix model .....	47
9.8	Comparison of the 2D-cylinder model and the 3D-helix model .....	49
10	EURECAT/ global field simulation .....	50
11	Discussion and Results .....	55
12	Outlook .....	56
12.1	Diameter Variation .....	57
12.2	Pitch Variation .....	59
13	Appendix .....	LXI
13.1	Material Properties .....	LXI
13.2	Sensorpoint data .....	LXII



## List of Figures

Figure 1: Overview of the GEOFIT structure [1] .....	2
Figure 2: Open Loop System (left) and Closed Loop System (right) [3] .....	4
Figure 3: Horizontal slinky loops .....	6
Figure 4: Horizontal spiral.....	6
Figure 5: Vertical basket .....	6
Figure 6: Vertical slinky loops .....	6
Figure 7: Overview of different system parameters of Spiral Type GHEX [10].....	7
Figure 8: Permeability of systems [17].....	9
Figure 9: steady state (left) and transient (right) heat transfer of a wall [18] .....	13
Figure 10: Area of the heat conducting body with the volume $V$ , the surface element $dA$ and with the outwardly directed normal-vector $n$ [16] .....	16
Figure 11: Defined Wall Temperature (left), given Heat Flux Density (center) and Heat Transfer Condition (right) [16].....	21
Figure 12: Overview of the testing strategy [19] .....	22
Figure 13: Block diagram concept of the experimental setup [19] .....	23
Figure 14: CAD Model of the experimental test site [19].....	24
Figure 15: Description of the 1D rod model .....	25
Figure 16: Gauss distributed heat source $q(x)$ .....	27
Figure 17: Comparison of the numerical Python® algorithm and the Fluent® code .....	28
Figure 18: Comparison of the numerical Python® algorithm and the analytical solution [6] .....	28
Figure 19: Parameters of the heating cable [19] .....	29
Figure 20: ANSYS® Workbench Structure.....	29
Figure 21: CFD Model.....	30
Figure 22: Dimensions of the box [19] .....	30
Figure 23: Mesh refinement and growth factor .....	31
Figure 24: Mesh on the heating cable .....	31
Figure 25: Number of elements over the growth rate (GR) .....	32
Figure 26: Polar coordinate system to describe the sensorpoint location [19].....	33
Figure 27: 3D Plot of the sensorpoint location [21] .....	34
Figure 28: Temperature distribution of the 2D Cylinder Model .....	35
Figure 29: Height in Z over temperature T of the experimental data [21].....	36
Figure 30: Comparison of simulation and experiment @ t+24h .....	37
Figure 31: Comparison of time-step 10s and time-step 100s .....	39
Figure 32: Comparison of time-step 10s to time-step 1000s .....	39
Figure 33: Comparison of time-step 10s to time-step 10000s.....	39
Figure 34: Comparison of SOI5 and SOI100 .....	40
Figure 35: Local mesh refinement of sensorpoint o33 with SOI5 .....	41
Figure 36: Variation of different thermal diffusivities $a$ .....	42
Figure 37: Comparison of different thermal diffusivities .....	42
Figure 38: Variation of the thermal diffusivity on the scaled 1D rod model.....	43
Figure 39: Variation of the density $\rho$ .....	44

Figure 40: Temperature of different heat transfer coefficients on T-t.....	45
Figure 41: Power input of 390W into the cylinder model .....	46
Figure 42: Temperature Comparison of 3D Simulation and Experiment @t+24h (Power-input= 280W) .....	47
Figure 43: Simulation and experiment results from fibre-optic temperature sensors at steady-state [6].....	48
Figure 44: Comparison of 2D cylinder model and 3D helix model .....	49
Figure 45: Eurecat cylinder model .....	50
Figure 46: Diameter of the cylinder inside the box .....	50
Figure 47: Position of the implemented cylinder in the box (X= 85mm and Y= 105mm) .....	50
Figure 48: Mesh refinement and growth rate .....	51
Figure 49: Mesh refinement on the heating cable.....	51
Figure 50: Grid view of the 3D Mesh model (left) and zoom onto the heating cable mesh (right).....	51
Figure 51: Single Point Comparison @timestep 60, 180, 840 (Timestep size 1000s) .....	52
Figure 52: Fibreoptics sensorpoints on cylinder_outer_jacket.....	52
Figure 53: Fibreoptics Sensorpoint height over temperature @t+60, t+180 and t+840 timesteps (timestep-size = 1000s) .....	53
Figure 54: Negative heatflux through the cylinder walls over time.....	53
Figure 55: Contour plot @ t+60, @ t+180 and @ t+840 timesteps (timestep-size = 1000s) .....	54
Figure 56: Contour plot of the cylinder_outer_jacket @ t+60, @ t+180 and @ t+840 timesteps (timestep-size = 1000s) .....	54
Figure 57: Parameters of the helix [19] .....	57
Figure 58: Loop-diameter = 280mm (topleft); Loop-diameter = 350mm (topright); Loop-diameter = 437,5mm (bottom-left; Jacket of the cylinder (bottom-right) .....	57
Figure 59: Heatflux through the jacket with varying diameter of the loop .....	58
Figure 60: Loop-pitch = 125mm (topleft); Loop-pitch = 100mm (topright); Loop-pitch = 80mm (bottom-left); Jacket of the cylinder (bottom-right) .....	59
Figure 61: Heatflux through the jacket with varying pitch of the loop .....	60
Figure 62: specific heat capacity of dry sand over temperature T [21].....	LXI
Figure 63: thermal conductivity of dry sand over temperature T [21].....	LXI
Figure 65: Mean values of the thermal properties and uncertainty @ T=20°C .....	LXI

## List of Tables

Table 1: Variation of thermal soil-properties in 2D .....	42
Table 2: Variation of normalised thermal soil-properties in 1D.....	43
Table 3: Temperature comparison @ t+24h .....	48
Table 4: Parameters of the sensorpoint helix .....	LXII
Table 5: Location of the sensorpoints i13, m23, o33 in the model domain .....	LXII

## List of abbreviations & symbols

The following list describes all the abbreviations and symbols that will be later used within this document.

<i>AIT</i>	.....	Austrian Institute of Technology
<i>BC</i>	.....	Boundary Conditions
<i>BHE</i>	.....	Bore Hole Heat-Exchanger
<i>CFD</i>	.....	Computational Fluid Dynamics
<i>CLS</i>	.....	Closed Loop Systems
<i>GHE</i>	.....	Groundsource Heat Exchanger(s)
<i>GSHP</i>	.....	Ground Source Heat Pump
<i>HEX</i>	.....	Heat Exchanger
<i>HFM</i>	.....	Heat Flow Meter
H2020	.....	Horizon 2020
<i>OLS</i>	.....	Open Loop Systems
<i>PDE</i>	.....	Partial Differential Equation
<i>R&amp;D</i>	.....	Research and Development
<i>SOI-Tool</i>	.....	Sphere of Influence – Tool
<i>SI</i>	.....	Système International
<i>TRT</i>	.....	Thermal Response Test
<i>WP(s)</i>	.....	Work Package(s)
$\alpha$	.....	Heat Transfer Coefficient [ $\text{W m}^{-2} \text{K}^{-1}$ ]
$\lambda$	.....	Thermal Conductivity [ $\text{W m}^{-1} \text{K}^{-1}$ ]
$\rho$	.....	Density [ $\text{kg m}^{-3}$ ]
$\nabla^2$	.....	(also written $\Delta$ ) Laplace Operator
$a$	.....	Thermal Diffusivity [ $\text{m}^2 \text{s}^{-1}$ ]
$c_V$	.....	Specific Heat Capacity at constant Volume [ $\text{J kg}^{-1} \text{K}^{-1}$ ]
$c_p$	.....	Specific Heat Capacity at constant Pressure [ $\text{J kg}^{-1} \text{K}^{-1}$ ]
$i_e$	.....	Density of the Current [ $\text{A m}^{-2}$ ]
$m$	.....	Mass [kg]
$\vec{n}$	.....	Area normal vector
$q_i$	.....	Specific Yield [ $\text{W m}^{-3}$ ]
$\dot{q}$	.....	Heat flux density [ $\text{W m}^{-2}$ ]
$Q$	.....	Heat [J]
$r_e$	.....	Resistivity [ $\Omega\text{m}$ ]
$t$	.....	Time Coordinate [s]

---

$T$	.....	Temperature [K]
$\Delta T$	.....	Temperature Difference [K]
$T_{Fluid}$	.....	Temperature of the Fluid [K]
$T_i$	.....	Initial Temperature [K]
$T_W$	.....	Wall Temperature [K]
$u$	.....	Specific Internal Energy [J kg <sup>-1</sup> ]
$U$	.....	Internal Energy of a System [J]
$U_E$	.....	Final State of a System
$U_A$	.....	Initial State of a System
$\Delta U$	.....	Change of Internal Energy from one State to the other [J]
$V$	.....	Volume [m <sup>3</sup> ]
$W$	.....	Work [J]
$W_V$	.....	Volume Work [J]
$W_{diss}$	.....	Dissipated Work [J]
$(x, y, z)$	.....	Space Coordinates [m]

# 1 Introduction

As climate change in the Anthropocene is one of the biggest challenges in the 21<sup>st</sup> century, humanity has to think about sustainable ways of providing energy. The building industry is known as an energy intensive sector and responsible for over a third of Europe's annual CO<sub>2</sub> emissions. Thusly, heating and cooling buildings is recognized as a field with high potential in reducing carbon dioxide. Modern heat pump technologies with their ability of cooling in summer and heating in winter (by reversing the heat transfer process) meet requirements perfectly. [1]

To provide a framework for the efficient integration of low emission technologies, many well-known European research institutes work together within an international project, called GEOFIT. This project is funded by the European Union's Horizon 2020 programme. Overall goal is to search for novel drilling techniques, site-inspections tools, monitoring techniques and new heat pump components. To demonstrate the practical maturity, energy demand of five European demonstration sites in four different countries is tracked and reduced by about 60%. [1]

GEOFIT is split into different work packages (WPs). WP3 as part of this master thesis deals with the design and the development of novel heat exchanger configurations within a closed loop system (CLS). The objective of WP3 is to examine basket and slinky loop ground source heat exchanger (GHE) of different geometric configurations in three different soil types to gain a better understanding of these unconventional compact shallow ground source heat exchangers. A lack of robust design methods and missing data sets for parameterization in terms of dimensioning GHE lead to oversizing effects. These effects have a negative influence on installation costs and market acceptance and customer risks. Due to the complexity of certain systems (varying boundary conditions, inhomogeneous soil properties etc.) the assumption of coefficients will be improved by using simulations in future. [1]

Of all compact GHE types developed in the past, the vertical coil heat exchangers (also called: earth baskets) are a good compromise between a large area of implementation (meandering pattern) and huge depths (vertical borehole) which correlate with high space requirement or high investment costs. Installation depths of an earth basket are less than 5 m, which lead to low installation costs. Due to this fact, earth baskets do not have a groundwater impact, which makes approval procedures fast. Therefore, earth baskets cover a lot of requirements for geothermal retrofitting of residential housing especially in dense urban area with a complex infrastructure. *Figure 1* shows the structure of GEOFIT within the H2020. [1]

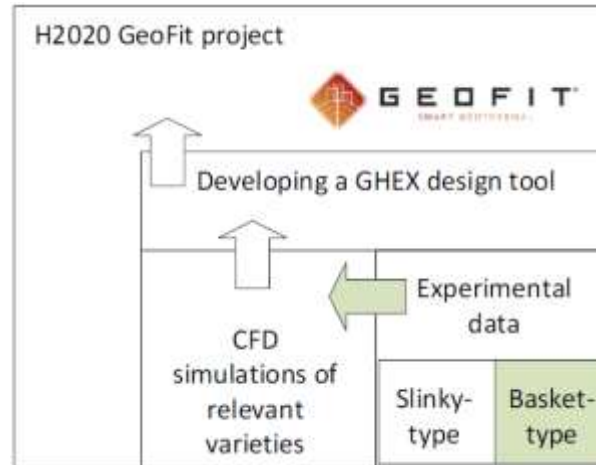


Figure 1: Overview of the GEOFIT structure [1]

After the explanation of the state of art in *chapter 3*, theory of heat conduction is presented in *chapter 4*. To understand the complex process of heat extraction/injection of earth baskets and the impact of the soils properties in reality, a simulation model, inspired by an existing experimental setup, is created. This experimental setup and the associated testing strategy is explained in *chapter 5*. This model generates the spatial- and time-dependent temperature distribution while injecting heat into the surrounding soil. The heat source in the model is realized by help of an electric wire, which is emitting a constant heat-flux into the system. To minimize computational effort to an acceptable dimension, time-step variation and cell reduction analysis are performed. Additionally, the 3D helix-model is simplified to a 2D cylinder-model. A simplified 1D rod-model helps to compare the numerical CFD Fluent code to the analytical solution of the general Fourier heat equation. The validation of the numerical ANSYS® code is presented in *chapter 6*. The following *chapter 7* will describe the setup of the simulation model in brief.

While *chapter 8* presents comparisons of experimental temperature field and simulation results, further CFD simulations based on the physical behaviour also provide information about the influence of different thermal properties ( $\lambda$ ,  $\rho$ ,  $c_p$ ), which describe the soil's properties clearly. As initial comparisons in this work showed clear deviations of experimental- and simulated temperature distribution, the origin had to be found. Further parameter variations allow to understand the influence of changing properties on the temperature distribution. Results are shown and discussed in brief in *chapter 9*.

Near field CFD simulation data is afterwards prepared as part of this thesis. It is used in a global far-field simulation, which is performed by the research partner EURECAT and presented in *chapter 10*. As individual earth baskets are mostly installed in defined arrangements, an understanding of the thermal interaction of individual baskets within those arrangements is essential. Later in *chapter 11* an attempt is made to answer following questions:

1. How can the simulation model be optimally adapted to ensure high resource efficiency? Which adjustments can be made?
2. Which material parameters ( $\lambda$ ,  $\rho$ ,  $c_p$ ) describing the thermal diffusivity, affect the temperature field in which way?
3. What can be said about the boundary conditions and their influence on the temperature field?
4. What is the possible origin of the temperature deviation in first comparisons of experiment and simulation? Can the deviation be attributed clearly or is it a combination of several factors?

Since it is assumed that geometrical configurations have a strong impact onto the thermal performance of earth baskets, a final variation of the slope and pitch length is performed. The Visualization of these data should provide a fundament for further scientific discourse to help optimizing shallow ground source heat exchangers as part of heat pump systems. Plots of the resulting heat fluxes are shown in *chapter 12*.

## 2 GEOFIT Objectives

As the installation process of BHE systems ask for long approval procedures while being linked to high drilling costs, market asks for cheap and compact alternatives for the retrofitting of existing buildings. To rise market acceptance and minimized customer risks oversizing of future GHEX must be eliminated too. [1]

If talking about retrofitting buildings, technical difficulties arise when coupling heat pumps with existing high temperature heating systems. The GEOFIT project intends to mitigate these hindrances through the following goals: [22]

1. Innovative geothermal systems, whereby the systems are specifically developed for geothermal based retrofitting. This encompasses an optimisation and integration of the geothermal system's components, as well as novel heat exchange concepts. Furthermore, the project will incorporate cost effective heat pumps, innovative heating and cooling components, as well as progressive IT control and monitoring technologies.
2. Integrate advanced methods of work site inspection, such as ground research, buildingstructural monitoring, Thermal Response Test (TRT) methods and work site characterisation. The approach used to achieve this is a multi-stakeholder and collaborative method, grounded predominantly on integrated delivery projects.
3. For the stock of existing buildings in Europe, the goal is to implement a global, energy efficient retrofitting strategy.

### 3 State of the Art

*Chapter 3* will give an overview of the current situation of geothermal heating systems and the status quo of scientific research performed in that field. *Chapter 3.1* gives an overview of Ground Source Heat Exchanger systems while *Chapter 3.2* focusses on Low Depth Spiral Heat Exchanger Types. Finally *Chapter 3.3* gives a good overview of main parameters that have a strong effect onto thermal performance of geothermal heating systems.

#### 3.1 Ground Source Heat Exchangers

Generally two main types of ground source heat exchangers must be differentiated.

So called Open Loop Systems (OLS) extract and reinject water stored in a huge aquifer in the underground. Typically two separated wells have to be drilled into the underground. These systems are also called: ground-water systems. [2]

Closed Loop Systems (CLS), which are also known as ground-coupled systems, operate with help of continuous pipe loops that are placed either horizontally or vertically in the ground. A circulating heat carrier extracts or reinjects heat into the surrounding soil. Most applications use the latent heat of the circulating heat carrier. [2]

*Figure 2* shows an OLS (left) and a CLS (right) in vertical configuration.

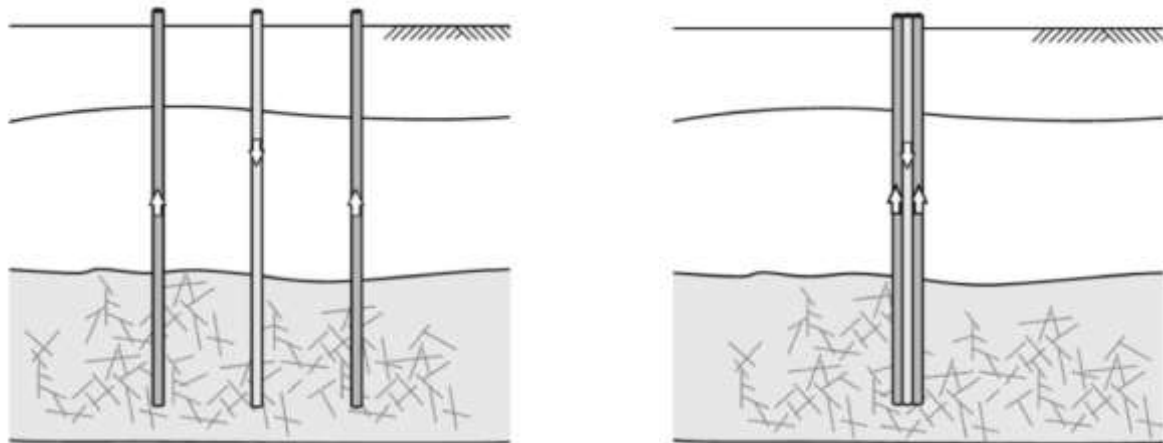


*Figure 2: Open Loop System (left) and Closed Loop System (right) [3]*

Many systems used all over Europe are so called Borehole Heat Exchanger (BHE) systems. With more than two decades of R&D focussing on BHE, this technology is already well-established on the market. Design and installation criteria are well developed, which allows, that a large number of these systems are operating in countries like Germany, Switzerland, Austria, Sweden, Denmark and France for example. [2]

The installation depths of these types range between 100 and 300 m. [4]



The application of these systems is becoming more commercial and industrial. Nevertheless they also have some disadvantages. They exhibit relatively high initial costs due to the required drilling process and the fact that deep wells are needed. This is not always an option in complex infrastructures. [1]

Therefore, an initiative was set up to work on the reduction of drilling costs and required land area. The aim is to focus research work on Low Depth Spiral Heat exchanger types. These ones are attractive, because they offer the lower total costs as well as the higher renewable contribution while allowing lower spatial requirements compared to existing surface collectors [5]. Especially space requirements can be a limiting factor in dense urban environments. It is also possible that the drilling depth is limited by law as in the Netherlands for example. [1]

While in small systems, like residential buildings, dimensioning parameters are usually estimated larger, systems ask for accurate data to avoid oversizing. Thermal conductivity for example is measured in situ with TRTs. The TRT determines the effective thermal conductivity of the underground, including conductivity and convection in permeable layers with groundwater. [4] One of the limiting factors, in terms of calculating more “complex” structures, like earth baskets and slinky type heat exchangers, is the non-existence of standardised TRT methods. This makes contractors and installers choose other types of heat exchangers with standardized TRT methods as the use of non-standard configurations is an extra cost, since each time a specific TRT method must be designed. A universal design tool for horizontal and vertical spiral GHEX has not been reported yet. [6] [7]

### 3.2 Low-Depth Spiral Heat Exchanger Types

Earth baskets and spiral probes are a combination of straight- and slinky probes. All of them are buried below the frost line at a depth of approximately 2.5 to 5 m depending on the region. Both, slinky collectors and spiral ones can be operating in vertical or horizontal position. Following rough installation parameters are common [8] :

**Horizontal slinky-loops (Figure3):** Installation in trenches of 2 x 1.5 m (width x depth). Overlapping between no overlapping to half of the diameter.

**Horizontal spiral (Figure4):** Installation in trenches of depths up to 5 m and a coil diameter between 0.2 and 0.5 m.

**Vertical spiral/basket (Figure5):** Installation in boreholes of depths up to 5 m and a coil diameter between 0.2 and 0.5 m.

**Vertical slinky-loops (Figure6):** Installation in trenches of 0.5 m width. Overlapping between no overlapping to half of the slinky diameter.

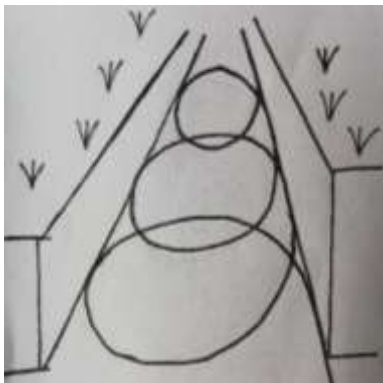


Figure 3: Horizontal slinky loops

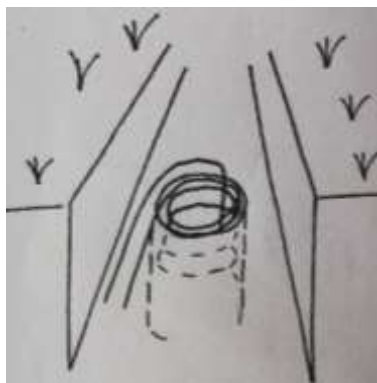


Figure 5: Vertical basket

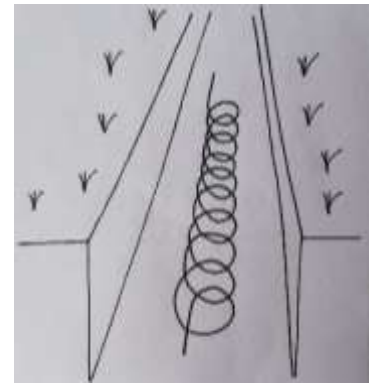


Figure 4: Horizontal spiral

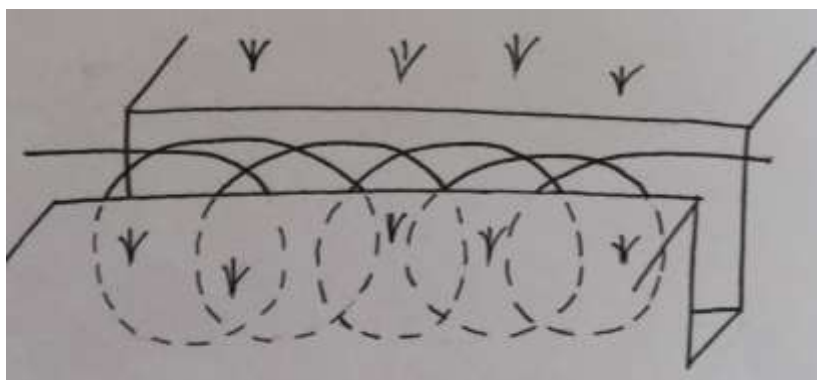


Figure 6: Vertical slinky loops

The heat transfer medium inside the GHEX (mostly water with glycol) circulates through HDPE- or copper-pipes, while extracting or injecting heat into the surrounding soil.

If spiral and slinky type heat exchangers are compared, spiral ones ask for less space-requirements. During operation an important circumstance to be mentioned is freezing effects especially at the inner zones of the baskets. [8]

These freezing effects, lead to a significant increase in the amount of energy that can be extracted, since *latent heat* is released during the phase change (approx.  $0.09 \text{ kWh kg}^{-1}$ ) and thermal conductivity of ice (approx.  $2.2 \text{ W m}^{-1} \text{ K}^{-1}$ ) is significantly higher than thermal conductivity of water (approx.  $0.6 \text{ W m}^{-1} \text{ K}^{-1}$ ). [9]

As the properties of the surrounding soil have a great impact onto thermal performance of shallow ground source heat exchanger systems, most important parameters are presented in the next chapter.

### 3.3 Influence of system parameters:

Literature either covers horizontal heat exchangers in different configurations (linear, slinky and helical) in shallow depths or vertical ones in depths  $> 10 \text{ m}$ . From 2010 to 2018 most of the shared studies have been performed on base of numerical methods (50%), while experimental investigations cover 23% and analytical ones 21%. The rest covers optimization work. [2]

As a GHE is in thermal interaction with the surrounding soil, a figure with the interacting parameters is presented. This figure is inspired by [10]. Further literature research focuses mainly on the ground temperature, the thermal properties of the soil and the geometric configuration of different GHEX. The parameters relevant to this work have been marked in red in *Figure 7*.

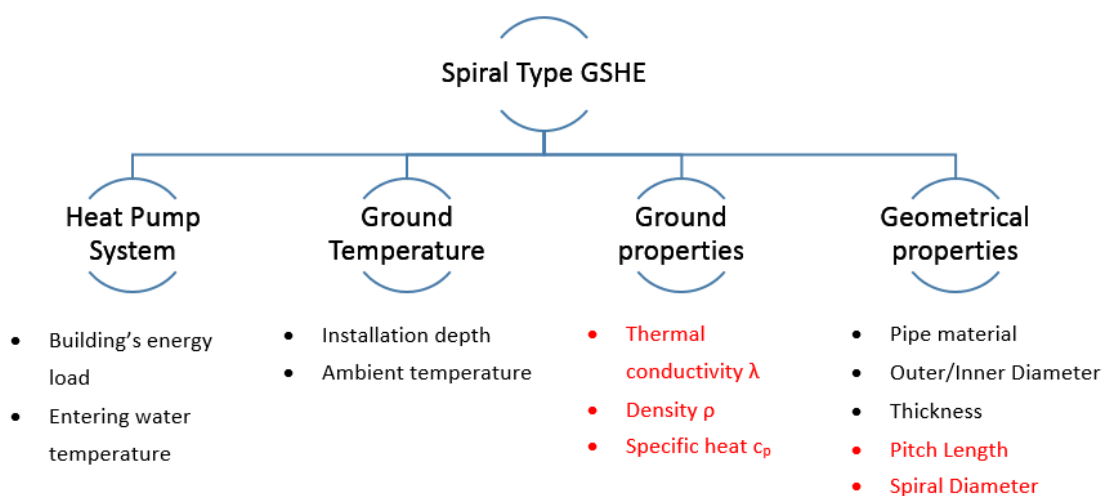


Figure 7: Overview of different system parameters of Spiral Type GHEX [10]

### 3.3.1 Ground Temperature

As the focus of this work is to study the influence of geometrical configurations and the impact of soil properties on thermal performance, varying ground temperature is not considered in the model. The boundary conditions (BC) of the simulation model are assumed to be constant over space and time.

### 3.3.2 Ground properties

The thermal conductivity  $\lambda$  has the most significant influence onto the performance of GHE besides  $\rho$  and  $c_p$ . The soil's thermal conductivity is highly depending on the moisture content. [11] [12] [13] [14]

### 3.3.3 Geometrical properties

If talking about geometrical properties, pitch length and spiral diameter (*Figure 7* right in red) are in the focus.

The spiral vertical pipe configuration has the highest efficiency-rate in terms of extracting and reinjecting heat into the soil compared to other configurations. [15]

Vertical heat exchangers are less sensitive regarding ground temperature fluctuations [13]. Further research on the optimal pitch length is needed. [5]

Experimental results lead to the conclusion, that helical shaped heat exchangers have to be preferred compared to others. [11]

If talking about pitch length variation, optimal pitch length is in between a maximum, where thermal performance converges, and a minimum pitch length, where thermal interference is dominant and limiting the performance. The spiral diameter does not significantly affect the thermal performance. [10]

Similar results are known for slinky loop heat exchangers. [13]

## 4 Theory of Heat Conduction

Heat transfer is an important part of thermodynamics and deals with thermal energy transport processes and their mathematical description. This chapter explains the practical implications of thermodynamics, such as the balance of energy and the definition of the 1<sup>st</sup> and 2<sup>nd</sup> Law of Thermodynamics. The theoretical principles in *chapter 4* are translated and summarized based on [16] if not marked explicitly.

### 4.1 Classification of systems

Thermodynamics can also be described as a “general theory of energy” within physics. The task of thermodynamics is to develop methods to help describing transfer and conversion of energy in general terms. This is mainly done by help of two scientific facts: the 1<sup>st</sup> and 2<sup>nd</sup> Law of Thermodynamics. [16, 17]

Basically, one can differentiate between three types of systems, which are defined by the characteristics of their system boundaries. Per convention, energy that is supplied to a system is signed with (+), while energy that is removed from a system is marked with (-).

- (a) **Fully-closed system** (no transfer of mass  $m$ , work  $W$  or heat  $Q$ )
- (b) **Closed system** (no transfer of  $m$ , transfer of  $W$  and  $Q$  possible)
- (c) **Open system** (allows  $m$ -,  $Q$ - and  $W$ - transfer)
- (d) **Adiabatic/Heat insulated system** (allows  $m$ - and  $W$ - transfer, no  $Q$  transport across the system boundaries)

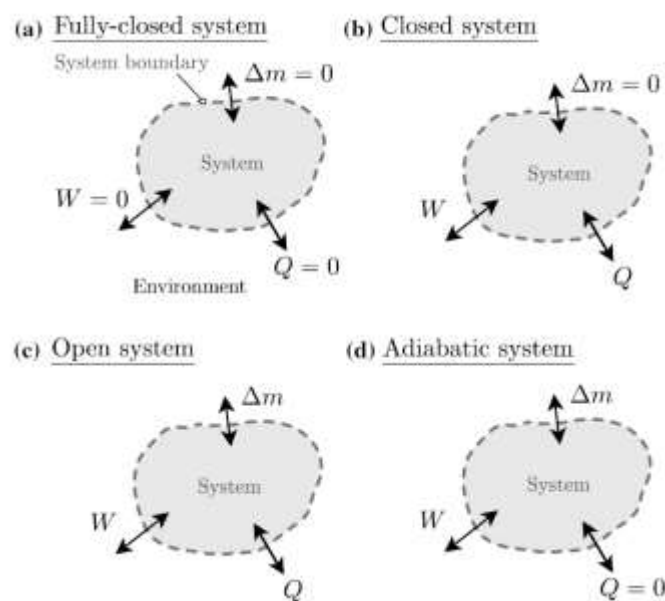


Figure 8: Permeability of systems [17]

Since no mass transfer but a possibility of energy transfer across the boundaries is expected in the experimental setup, it can be seen as a closed system. Further simplifications are possible and discussed in later chapters.

## 4.2 First Law of Thermodynamics

The 1<sup>st</sup> Law of Thermodynamics is written in many different forms. Basically, it provides a statement about the conservation of energy. A possible formulation that is valid for the closed system is:

$$\Delta U = Q + W \quad (1)$$

Equation ( 1 ) describes the energy balance of a closed system. It states, that the change of internal energy ( $\Delta U$ ) is equal to the energy transported beyond the system boundaries in form of heat ( $Q$ ) and work ( $W$ ). While the temperature-level describes the state of certain system,  $Q$  changes the energy of the system. While the temperature  $T$  is called a *thermal state value*,  $Q$  is called a *process variable*. Energy that is transported across the system boundary is called *heat*  $Q$ , if the energy transport is caused by a temperature difference between the system and its environment.

The energy of the closed system is known as internal energy  $U$  (ignoring the potential and kinetic energy). If a system is transferred from state A with a certain internal energy  $U_A$  to the final state E with  $U_E$ , the internal energy increases according to Equation ( 2 ) :

$$\Delta U = U_E - U_A \quad (2)$$

The internal energy is also a state variable which is defined by the current state of the system but not depending on the path, the system reached this state (path-independent variable).

The *work*  $W$  performed is splitted into the volume work  $W_V$  and the dissipation work  $W_{diss}$ .

$$W = W_V + W_{diss} \quad (3)$$

If a gas is compressed with a piston, *volume work* is performed on the *closed system*. *Dissipation energy* is the devaluation of energy caused by friction. Parts of  $W$  are converted irreversibly into *thermal energy*.

### 4.3 Second Law of Thermodynamics

This law of nature defines the direction of heat transport. It says that:

*“Heat can’t be transported from a system of lower temperature to a system of higher temperature by itself.” [16]*

In other words: heat flows voluntarily into the direction of lower temperature levels. Thermodynamics itself does not tell us how the heat will be transferred or how fast and intensive the process of heat transfer will be. Its task of *heat transfer theory* to deal with these issues.

### 4.4 Principles of Heat Transfer

The task of *heat transfer theory* as a sub-area of *thermodynamics* is the investigation and description of heat transport processes, which are always caused by a temperature difference. There are three types of heat transport mechanisms:

- Heat conduction
- Heat convection
- Heat radiation

*Heat conduction* is the transport of heat through the particles of a **solid or immobile** media, caused by a temperature gradient or a temperature gradient.

*Convection* takes place through a combination of heat conduction and particle movement of the medium. Convection therefore only takes place in **moving, fluid media** (gases or liquids). If the fluid movement is caused by external influences such as pumps or fans, it is called *forced convection*. In contrast, *free convection* is present, when the fluid movement is only caused by resulting differences in density and temperature.

In the case of *heat radiation*, energy is transported by means of electromagnetic waves. Thus *heat radiation* can also take place in a vacuum and is **not bound to a substance**. Every object emits energy by means of electromagnetic waves. If electromagnetic radiation hits a body, it is partly absorbed, reflected or transmitted. Although *heat radiation* is a heat transport form that is not bound to a substance it depends on the material properties and its surface texture. The higher temperature levels are, the higher is the influence of *heat radiation*. This phenomenon is described by the *Stefan Boltzmann Law*.

Depending on the circumstances and the practical application, up to three different heat transport mechanisms are involved. In solids, heat transfer occurs mainly through *heat conduction* and partly through *radiation* (if the solid is sufficiently permeable to electromagnetic radiation). In liquid and gaseous media all three energy transport mechanisms are superimposed.

In the present master thesis the material which represents the medium, consists of solid and dry particles. The sand is considered to have homogeneous properties, while particles are immobile. Radiation- and convection processes are neglected within the model of the box. As the copper cable is surrounded by a HDPE sleeve, it must be prevented, that temperatures exceed the cables jacket's melting point of  $T = 140^{\circ}\text{C}$ .

#### 4.5 Principle of Heat Conduction

*Heat conduction* is the transport of energy as a result of atomic and molecular interaction of a solid or an unmoved liquid or gaseous medium under the influence of irregular temperature distribution (spatial temperature gradient). Thereby, molecules with higher kinetically energy transfers their energy to neighbouring molecules with lower kinetic energy. [16, 18]

This chapter describes the stationary (steady state) and transient (unsteady) *heat conduction* phenomenon inside a resting media. At the beginning the *Law of Heat Conduction* is worked out, which is generally known as the *Law of Fourier*. Furthermore Fourier's heat conduction equation is derived, which can be used to determine the temperature field  $T(x, y, z, t)$  in the resting medium. For this purpose, the *Law of Energy Conservation* is linked to *Fourier's Law*.

#### 4.6 Stationary/Transient Heat Conduction

The heat conduction itself can again be classified into two types: [18]

**Stationary Heat Conduction:** time-independent *heat conduction*. It is characterised by a temperature field that remains unchanged over time. The amount of *heat* supplied corresponds to the amount of *heat* removed. The heat flow is constant in this case. A stationary state is reached as soon as a body is in thermal equilibrium with the environment. [18]

**Transient Heat Conduction:** time-dependent *heat conduction*. The temperature field changes with passing time. The amount of *heat* supplied is greater or smaller than the amount of *heat* removed from the system. The heat flow is not constant. Time-dependent temperature



fields occur when the thermal conditions at the boundary surfaces of a body changes or heat sources or sinks are present. [18]

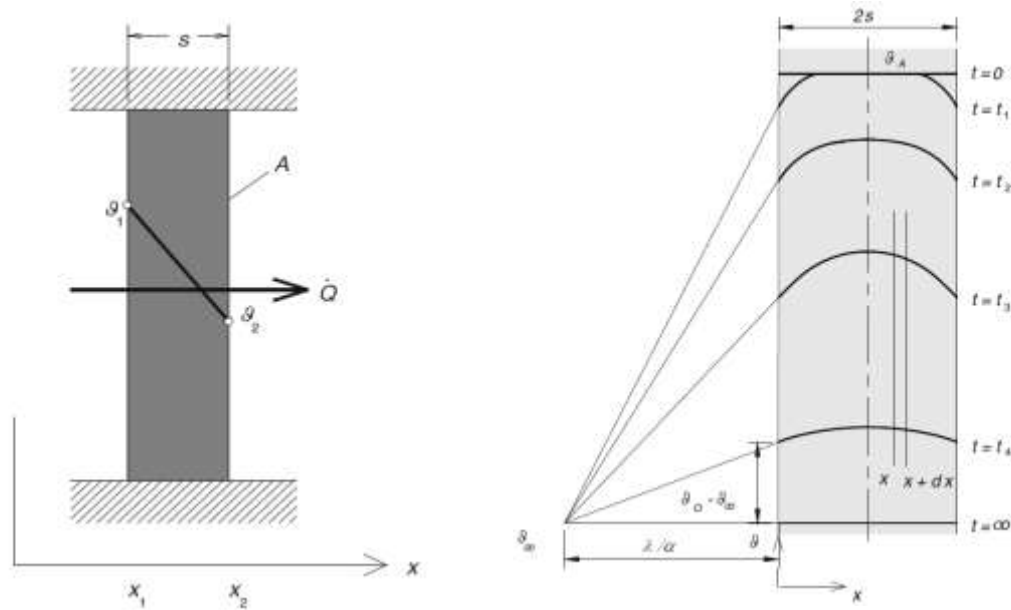


Figure 9: steady state (left) and transient (right) heat transfer of a wall [18]

#### 4.7 The Law of Fourier

The transport of energy in a heat-conducting media can be described by means of the heat flux density  $\dot{q}$  [ $\text{W m}^{-2}$ ].

$$\dot{q} = \dot{q}(x, t) \quad (4)$$

The reason for energy transport by heat conduction is a temperature gradient (spatial temperature difference) inside the material. The temperature changes from place to place and with passing time. The totality of temperatures is described by the temperature field, which is a function in space and time.

$$T = T(x, y, z, t) \quad (5)$$

There is a relation between  $\dot{q}$  and the temperature-distribution  $T$ . This law has been introduced by Biot (1816) and Fourier (1822) and is written in following form:

$$\dot{q} = -\lambda \text{grad}(T) \quad (6)$$

This relationship applies to any homogeneous, isotropic body and has been confirmed by precision measurements without any exception.

Equation ( 6 ) states, that heat flux density  $\dot{q}$  is proportional and opposite directed to the gradient of temperature  $grad(T)$ . The proportionality factor  $\lambda$  is called *thermal conductivity* [ $W\ m^{-1}\ K^{-1}$ ].

The (-) sign takes the 2<sup>nd</sup> law of thermodynamics into account, according to which  $Q$  only flows in directions of lower temperature.

The temperature gradient  $grad(T)$  mentioned above can also be written as  $\nabla T$ . It indicates the temperature difference in all three spatial directions and has the following form using Cartesian coordinates (x,y,z) describing the space:

$$\nabla T = gradT = \frac{\partial T}{\partial x} \vec{e}_x + \frac{\partial T}{\partial y} \vec{e}_y + \frac{\partial T}{\partial z} \vec{e}_z \quad (7)$$

In cylindrical coordinates (r, $\varphi$ ,z) it is written in the following form:

$$\nabla T = gradT = \frac{\partial T}{\partial r} \vec{e}_r + \frac{1}{r} \frac{\partial T}{\partial \varphi} \vec{e}_\varphi + \frac{\partial T}{\partial z} \vec{e}_z \quad (8)$$

For specific applications, a two-dimensional or even one-dimensional temperature gradient is a sufficiently close approximation. This assumption is permissible, as long as dimensions of a body in y-direction and z-direction are much greater than the dimension in the x-direction for example.

## 4.8 Differential heat conduction equation

The basis for solving complex heat conduction problems, which go beyond the simple case of stationary, one-dimensional heat conduction, is a differential equation for determining the temperature field in a resting media. This equation is called *Fourier's heat conduction equation*.

In the following section the derivation of *Fourier's heat conduction equation* in its general form and the assumed boundary conditions are going to be explained.

### 4.8.1 Definition of the general equation

Solving a heat conduction problem equals the identification of the temperature field T

$$T = T(x, t) \quad (9)$$

in space  $(x, y, z)$  and time  $(t)$ . If the temperature field  $T$  is known, the heat flow  $\dot{q}$  at any certain point of the body can then be determined by using Fourier's law:

$$\dot{q}(x, t) = -\lambda \nabla T(x, t) \quad (10)$$

The temperature field  $T$  itself is obtained by solving a partial differential equation, the so-called *Fourier heat conduction equation*.

To derive the heat conduction equation, the 1<sup>st</sup> law of thermodynamics (conservation of energy) is applied to a *closed system*. The *closed system* is a continuous area of any size. The volume of this heat-conducting area is  $V$  [m<sup>3</sup>] and its surface is  $A$  in [m<sup>2</sup>]. The energy- and performance balance of the *closed system* can be written in form of ( 11 ) and ( 12 ):

$$dU = dQ + dW \quad (11)$$

$$\frac{dU}{dt} = \dot{Q}(t) + \dot{W}(t) \quad (12)$$

Based on the assumption that the considered body is solid, density changes, caused by pressure and temperature changes, may be neglected. By help of the simplification ( $\rho = \text{const.}$ ), the *internal energy*  $U$  [J] changes over time and equals:

$$\frac{dU}{dt} = \frac{d}{dt} \int_m u * dm + \frac{d}{dt} \int_m u * \rho * dV = \rho \int_m \frac{du}{dt} * dV \quad (13)$$

while:

$$dm = \rho * dV \quad (14)$$

Using the *specific heat capacity*  $c_v(T)$  [J/(kgK)] of the body at constant volume, the *specific internal energy*  $u$  [J/kg] of the body equals:

$$du = c_v(T) * dT \quad (15)$$

$c_p(T)$  is known as the *specific heat capacity* at constant pressure. Equation ( 16 ) applies to all solids and liquids.

$$c_v = c_p = c \quad (16)$$

By combining ( 13 ) and ( 16 ) the temporal change of the inner energy over time equals:

$$\frac{dU}{dt} = \rho \int_V c(T) * \frac{\partial T}{\partial t} * dV \quad (17)$$

To determine the heat flow  $\dot{Q}$  [W] over the surface A of the solid body, a differential sized area element  $dA$  of the body surface is considered. It's normal vector  $\vec{n}$  is directed outwards:

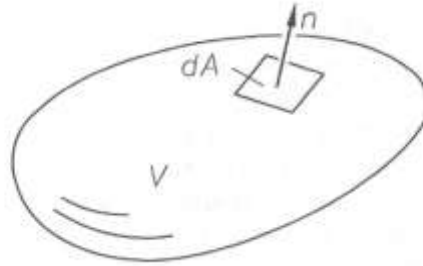


Figure 10: Area of the heat conducting body with the volume  $V$ , the surface element  $dA$  and with the outwardly directed normal-vector  $\vec{n}$  [16]

The differential sized *heat flow*  $\dot{Q}$  through  $dA$  is positive and can be written as follows:

$$d\dot{Q} = -\dot{q} * \vec{n} * dA \quad (18)$$

Although the vector of heat flux density is positive (directed into the body), the normal vector  $\vec{n}$  points outwards. This results in a negative scalar product. The heat flow over the entire surface of the solid body is therefore given by:

$$\dot{Q} = - \int_A \dot{q} * \vec{n} * dA \quad (19)$$

With help of the Gaussian integral theorem described by ( 20 ) the surface integral turns into a volume integral of the form ( 21 ):

$$\int_A (\vec{F} * \vec{n}) * dA = \int_V (\nabla * \vec{F}) * dV \quad (20)$$

$$\dot{Q} = - \int_V \nabla * \dot{q} * dV \quad (21)$$

The Total Power  $\dot{W}$  [W] consists of two parts –  $\dot{W}_V$  which causes a volume change and  $\dot{W}_{diss}$  which is dissipated inside the body. The following assumption applies to an incompressible body:

$$\dot{W}_{diss} = 0 \quad (22)$$

An power source term described by  $\dot{W}_{diss}$  can be realized by using a heating wire for example (ohmic resistor), which dissipates power as a result of an electric current through the resistor. In this process, electric energy is converted into heat. The wire acts as an internal heat source.

The performance of this dissipative (and therefore irreversible) energy conversion, can be described by:

$$\dot{W} = \dot{W}_{diss} = \int_V \dot{q}_i * dV \quad (23)$$

In case of (23)  $\dot{q}_i$  is the *specific yield* of the inner heat- source [ $W m^{-3}$ ]. If an electric resistor is used,  $\dot{q}_i$  is defined as follows:

$$\dot{q}_i = r_e * i_e^2 \quad (24)$$

While  $r_e$  is the electric resistance of the body in [ $\Omega m$ ],  $i_e$  is known to be the density of the current in [ $A m^{-2}$ ]. No matter if heat is externally supplied or generated by an internal heat source, it results in an increase of the internal energy of the body.

The final equation of  $dU/dt$  in (17),  $\dot{Q}$  in (21) and  $\dot{W}_{diss}$  in (23) are combined to Equation (25) and simplified to (26):

$$\int_V [\rho * c(T) * \frac{\partial T}{\partial t} + \nabla * \dot{q} - \dot{q}_i] dV = 0 \quad (25)$$

$$\rho * c(T) * \frac{\partial T}{\partial t} = -\nabla * \dot{q} - \dot{q}_i \quad (26)$$

If we now add the *Law of Fourier* ( 10 ) into ( 26 ), we obtain the differential equation to describe the temperature field  $T$  in a resting, isotropic and incompressible material with temperature-dependent material values  $c(T)$  and  $\lambda(T)$ . The general form of Fourier's heat conduction equation, can be written as follows:

$$\boxed{\rho * c(T) * \frac{\partial T}{\partial t} = \nabla[\lambda(T)\nabla T] + \dot{q}_i} \quad (27)$$

Equation ( 27 ) is a non-linear partial differential equation, since the material values are a function of temperature  $T$ . If the temperature  $T$  dependence of the thermal conductivity  $\lambda$  and the specific heat capacity  $c$  is neglected ( $\lambda = const., c_p const.$ ) equation ( 27 ) becomes a linear differential equation of the form ( 28 ) and ( 29 ):

$$\rho * c(T) * \frac{\partial T}{\partial t} = \lambda * \nabla^2 T + \dot{q}_i \quad (28)$$

$$\frac{\partial T}{\partial t} = \frac{\lambda}{\rho * c} \nabla^2 T + \frac{\dot{q}_i}{\rho * c} \quad (29)$$

The differential operator  $\nabla[\lambda(T)\nabla T]$ , which occurs in case of constant thermal conductivity  $\lambda$ , becomes  $\lambda\nabla^2 T$ , which finally corresponds to the Laplace operator. It can be written in form of  $\lambda\Delta T$ . Equal to the temperature gradient, the Laplace operator is also written in a corresponding form depending on the coordinate system describing the space spectrum.

Furthermore the thermal diffusivity  $a$  in [ $m^2 s^{-1}$ ] is defined in Equation ( 30 ):

$$a = \frac{\lambda}{\rho * c} \quad (30)$$

Finally, the thermal diffusivity is used in equation ( 31 ) and the differential equation for constant material values has following form:

$$\boxed{\frac{\partial T}{\partial t} = a\nabla^2 T + \frac{\dot{q}_i}{\rho * c}} \quad (31)$$

## 4.9 Simplifications and Boundary Conditions (BC)

For the application of the general Fourier heat conduction equation ( 31 ), a number of simplifying assumptions can be made in order to obtain a differential equation tailored to the respective test setting.

### 4.9.1 Simplifications

- the absence of a heat source/heat sink

$$\dot{q}_i = 0 \quad (32)$$

- a stationary temperature field  $T(t)$  (a time-independent state has already been established). This results in

$$\frac{\partial T}{\partial t} = 0 \quad (33)$$

- geometric conditions often allow a reduction of the spatial dimension. Heat conduction through a plane wall, for example, allows:

$$\frac{\partial^2 T}{\partial^2 y} = 0 \quad \text{and/or} \quad \frac{\partial^2 T}{\partial^2 z} = 0 \quad (34)$$

### 4.9.2 Boundary Conditions

Since *Fourier's heat conduction equation* determines the temperature field  $T$  only inside the body (control volume), more information is needed to specify the temperature field  $T$ . For this reason, the interaction of the control volume with the surrounding environment has to be defined in form of *Boundary Conditions (BC)*. While “BC of time/Initial conditions”) provide information about the starting time of the process, the “BC of space” provide information of the spectrum in space.

The initial condition determines the temperature at each point of a body, at a certain time. In the simulation this process is called *Initialisation*. Mathematically it could be written in following form:

$$T(x, y, z, t = 0) = T_i(x, y, z) \quad (35)$$

The spatial BCs contain information about the temperature of the body surface (described by  $T_w$ ), the heat flow through the body surface (described by  $\dot{q}$ ) or a convective interaction of the body and its environment (described by the *heat transfer coefficient*  $\alpha$ ). Three types of spatial BC have to be mentioned:

#### 4.9.2.1 Defined boundary temperature $T_w$

In this case (see *Figure11 (left)*), the temperature on the body surface is prescribed as a function of place and time. The heat flow over the body surface is not directly known and must be determined by using Fourier's law.

$$T_{wall} = T_w(x = 0, t) \quad (36)$$

#### 4.9.2.2 Defined heat flux density $\dot{q}_{wall}$

The heat flow orthogonal to the body surface is given as a function of time and space. The change of the temperature profile (in other words: The 1<sup>st</sup> spatial derivative of the temperature profile  $T$ ) is given in relation to the area normal  $\vec{n}$  (see *Figure11 (center)*). The temperature  $T$  itself is unknown. The heat input by solar radiation or by heated electric foils on the surface are popular examples. Although the heat flow itself is positive, the falling temperature profile results in a (-) sign in Equation (37).

$$\dot{q}_{wall} = -\lambda \frac{\partial T}{\partial x} |_{wall} \quad (37)$$

#### 4.9.2.3 Heat transfer condition

In this case, the body surface is in contact and interaction with another medium to/from which an energy flow is transmitted. The temperature of the surrounding medium is known. If it is a fluid media (gases, liquids), heat transfer takes place.



Under the assumption of a steady state (no heat accumulation), the convective heat flow in the fluid must be the same size as the heat transport through conduction in the body. This circumstance allows to combine ( 38 ) and ( 39 ) to Equation ( 40 ):

$$\dot{q} = \alpha(T_{Wall} - T_{Fluid}) \quad (38)$$

$$\dot{q} = -\lambda \frac{\partial T}{\partial x} |_{wall} \quad (39)$$

$$\alpha(T_{Wall} - T_{Fluid}) = -\lambda \frac{\partial T}{\partial x} |_{wall} \quad (40)$$

The heat transfer is characterised by the heat transfer coefficient  $\alpha$  in [ $\text{W m}^{-2} \text{K}^{-1}$ ]. In most cases,  $\alpha$  can only be determined experimentally, as it depends on many parameters (see *Figure11 (right)*).

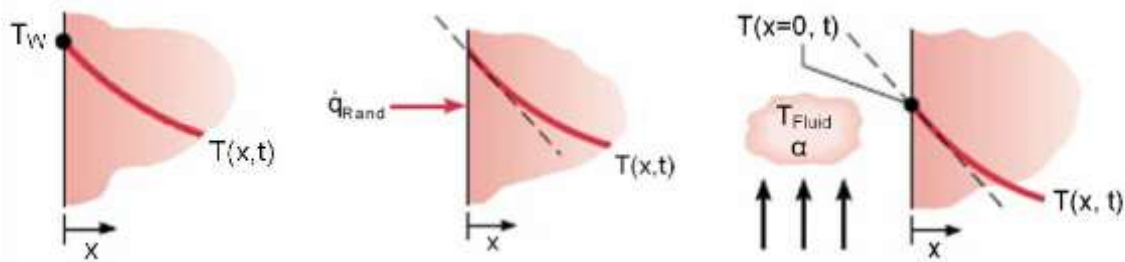


Figure 11: Defined Wall Temperature (left), given Heat Flux Density (center) and Heat Transfer Condition (right) [16]

## 5 Experimental site

This chapter will give a brief overview of the test strategy and will introduce the experimental setup.

### 5.1 Testing strategy

In order to create an experimental database, which can be used for further comparisons to CFD simulations, following parameter combinations for different GHEX systems were defined within the starting phase of the GEOFIT project.








	Vertical basket	Horizontal basket	Horizontal flat-lying	Horizontal flat-standing
Geometry types				
Soil types	Gravel bedding sand 	Soil sieved humus 	Loamy/clayey mixture 	
Heat flow rates	Heat extraction	Heat injection		

Figure 12: Overview of the testing strategy [19]

A total of four different geometry types in three different soil types are going to be investigated in course of the whole project.

For the beginning, heat injection is simulated by use of an electric heating cable, since effects of geometry changes are in focus for later on. This master thesis will focus on the physical behaviour of a vertical basket inside gravel bedding sand in heat injection mode. [19]

### 5.2 Experimental setup

The experiment was set up in a HD-PE plastic container with a total volume of 1 m<sup>3</sup>. A plastic grid acts as support structure for the heating cable helix, which is working as the GHEX. *Figure13* shows a block diagram of the experimental setup.

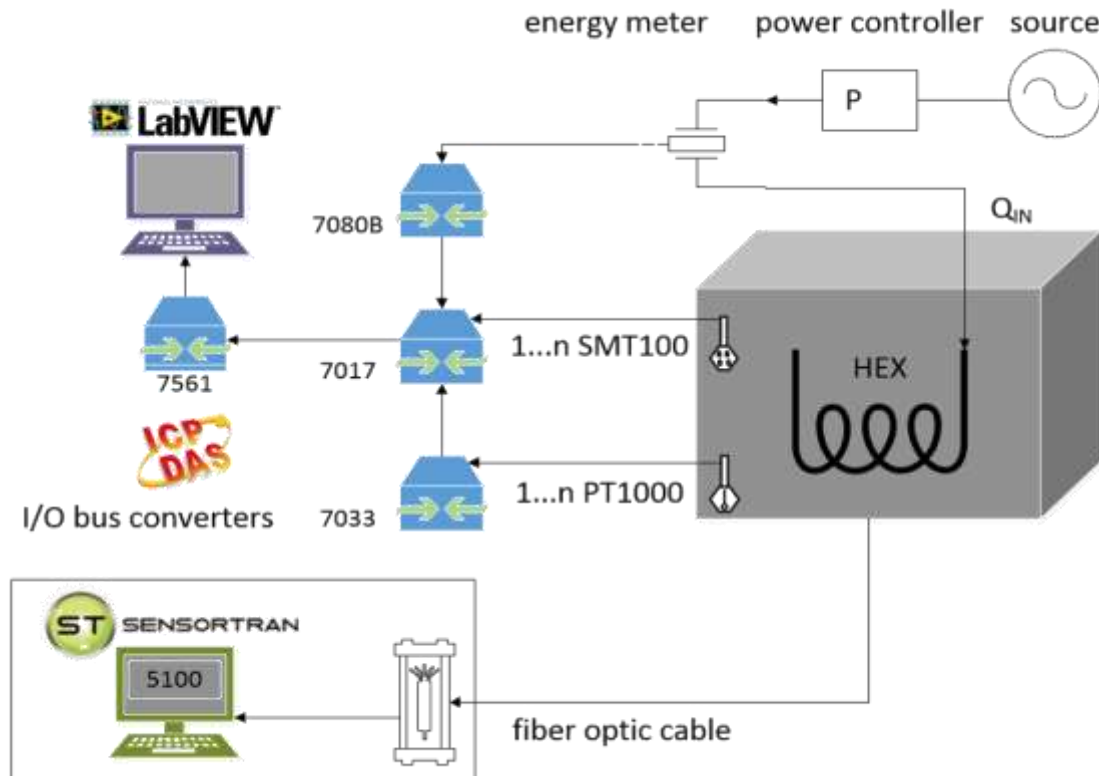


Figure 13: Block diagram concept of the experimental setup [19]

In order to measure temperature gradients in all directions, a measuring system based on PT1000 sensors and a Distributed Temperature Sensing (DTS) system were installed inside the box. DTS systems are widely used for vertical boreholes in the oil industry for example. Such systems provide a temperature profile along a fibre optic cable, while reducing the systemic influence of the sensors as much as possible due to the advantage of not having any supply lines to the sensors. The DTS cable is also mounted in a helical configuration onto the inner- and the outer side of the heating cable (see *Figure 14*).

The sensor lines on the container inner surface provide information about the boundary conditions. Additionally, SMT100 sensors (green) provide information about the moisture content of the soil as this parameter might have a huge influence on thermal conductivity according to literature. Both PT1000 and SMT100 sensors are located in one quarter of the box due to the symmetry of the setup.

The setup is placed in a climatic chamber to apply defined initial conditions and boundaries to the whole system. The bottom of the HD-PE box is insulated to reduce heat-losses.

The data is provided within a “.CSV” data file including a timestamp, length indicators and temperature data for each data point. The evaluation of the data-series is done by help of a Python® Code. The location of all measuring points is based on a Cartesian coordinate system with its origin in the bottom centre of the container. Following pictures show different views of the experimental setup.

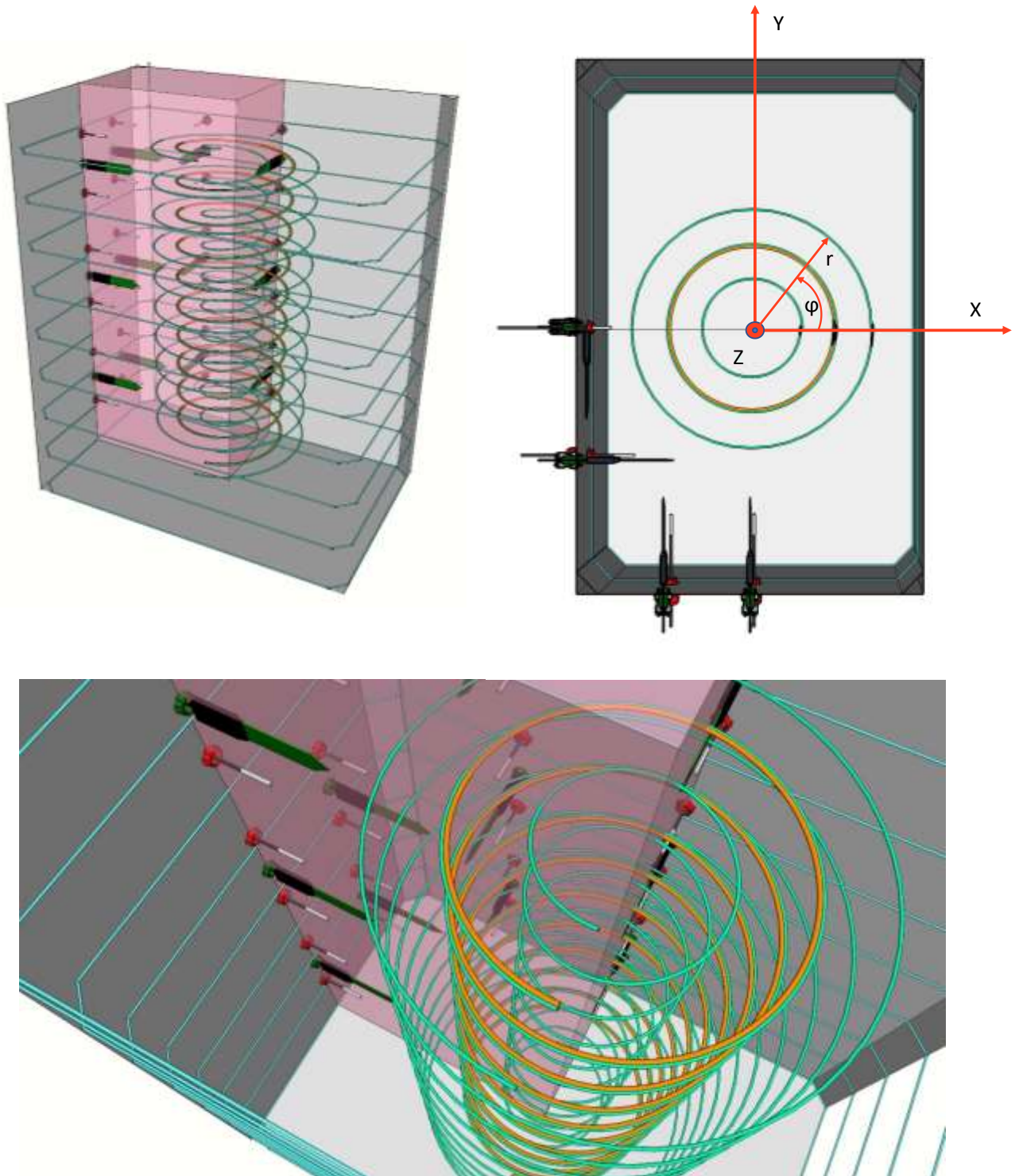


Figure 14: CAD Model of the experimental test site [19]

## 6 Validation of the numerical ANSYS Fluent Code

In order to display and check the validity of the numerical *ANSYS® Fluent* code, a simplified 1D rod model is used to compare analytical calculations with numeric solutions of the differential heat equation. While a python programme code calculates the numeric solution of a heat conduction problem, including a heat source in the middle, the boundary conditions on the left and right end of the rod are set to constant temperature. The heat source is described by a function  $f(x)$  of the rod's length coordinate  $x$  and has the form of a Gaussian distribution. A variation of the thermal rod-properties provide important insights into the influence of the thermal properties ( $\lambda$ ,  $\rho$  and  $c_p$ ) onto the distribution of the temperature field  $T$ .

### 6.1 1-D heat equation

To compare the *ANSYS® Fluent* code with a numerical and additionally an analytical solution, a 1D rod model is generated. For this purpose, a rod with standardised thermal properties is fixed between two walls that are hold at constant temperature  $T$ . The boundary temperature and material property values of the rod model do not attempt to represent real-life application. The values were chosen to reduce the mathematical complexity of the problem. [6]

The situation can be described graphically as follows:

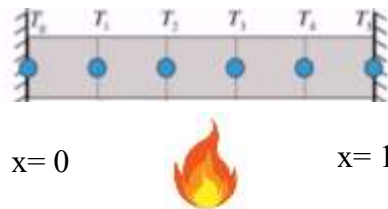


Figure 15: Description of the 1D rod model

To reduce the complexity of the system, the model is shown in its dimensionless form. In this case:

$$\zeta = \frac{x}{L_*} \quad (41)$$

The sensible choice for the characteristic length is  $L_* = l$  and represents the length of the rod. To solve this heat problem, more information is needed. While  $x$  is in the range:  $0 < x < l$ ,  $\zeta$  ranges from  $0 < \zeta < 1$ .

The solution of the 1D model is assumed to be steady. Starting temperature is set to  $(x, 0) = 0K^1$ , while boundary temperatures are set to a constant temperature  $T_0 = T_L$  and  $T_5 = T_R$ . The thermal properties of the rod are standardised. This leads to following assumptions:

$$\frac{\partial T}{\partial t} = 0 \quad T(x, 0) = 0K. \quad (42)$$

$$\frac{\partial^2 T}{\partial^2 y} = 0 \quad \frac{\partial^2 T}{\partial^2 z} = 0 \quad (43)$$

$$T(\zeta=0) = T_L = 0K, T(\zeta = 1) = T_R = 0K \quad (44)$$

$$\lambda = 1, \quad c_p = 1, \quad \rho = 1 \quad (45)$$

Some of this assumptions reduce the dimension of the general heat equation to:

$$0 = \nabla^2 T + \dot{q}_i \quad (46)$$

## 6.2 Definition of the heat-source

The heat source  $\dot{q}_i(x)$  is a function of the rod's length coordinate and is described by a Gaussian distribution of the following form:

$$\dot{q}_i(x) = A * e^{-\sigma(x-0.5)^2} \quad (47)$$

The maximum of the heat source function  $\dot{q}_i(x)$  is located in the middle of the rod at  $x = 0.5 m$ . The amplitude is defined by  $A = 1200W/m$  and a bell width of  $\sigma = 50 m^{-2}$ . A plot of the heat source over the length coordinate of the rod, can be seen in *Figure16*.

---

<sup>1</sup> If using a standardized rod model, temperature values can be adjusted to any value. The value of  $T = 0K$  was chosen, to guarantee better comparability.

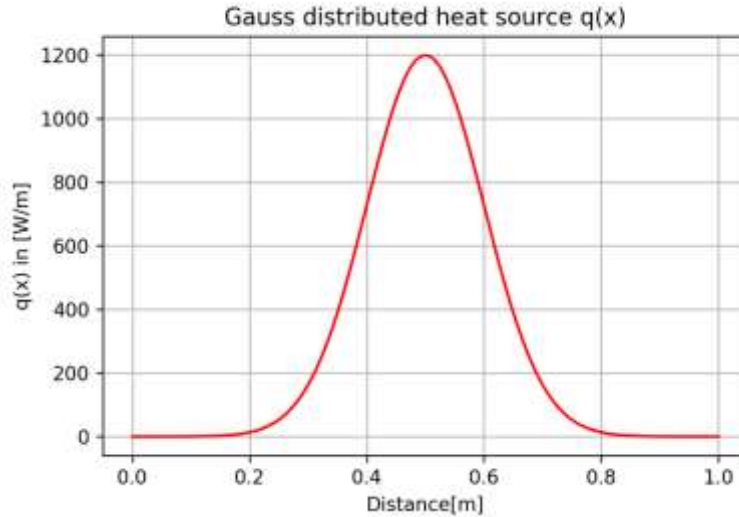


Figure 16: Gauss distributed heat source  $q(x)$

### 6.3 Comparison of a numeric solution and the ANSYS® Fluent algorithm:

To achieve a discretization of the domain-length, the rod has to be split up into a finite number of points. The set of linear algebraic equations is solved by help of *Python*®. As already mentioned the source term of the PDE is described by a Gaussian distribution. As the steady state solution is discussed, following PDE equation has to be solved:

$$\frac{d^2T}{dx^2} = -\frac{1}{a} * \dot{q}(x) \quad (48)$$

As the rod is subdivided into a number of  $n=100$  points ( $n-1$  intervals), the matrix will look like the following:

$$\begin{bmatrix} 1 & 0 & 0 & \dots & 0 \\ 1 & -2 & 1 & \ddots & 0 \\ 0 & \ddots & \ddots & \ddots & 0 \\ \vdots & \ddots & 1 & -2 & 1 \\ 0 & 0 & 0 & 0 & 1 \end{bmatrix} \begin{bmatrix} T_0 \\ T_1 \\ \vdots \\ T_{n-2} \\ T_{n-1} \end{bmatrix} = \begin{bmatrix} T_0 \\ -\Delta x^2 \times \frac{S}{k} \\ \vdots \\ -\Delta x^2 \times \frac{S_{n-1}}{k} \\ T_L \end{bmatrix} \quad (49)$$

The solution of the built-in Python solver is compared to the solution of the ANSYS® Fluent algorithm and visualized in *Figure17*. It can be seen that both algorithms provide the same solution (in sufficient accuracy). In other words: The validity of the ANSYS® Fluent code has been proven by the match of the curves. It has to be recognized that the maximum  $\Delta T$  of the rod, under certain conditions, is located in the center, which is physically plausible.

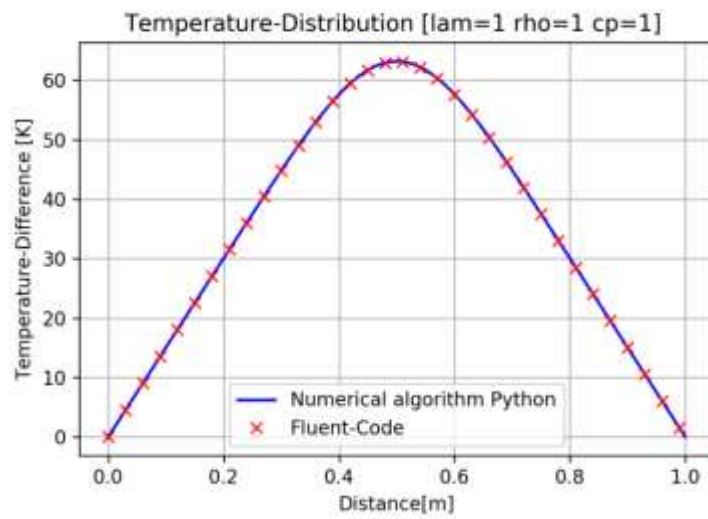


Figure 17: Comparison of the numerical Python® algorithm and the Fluent® code

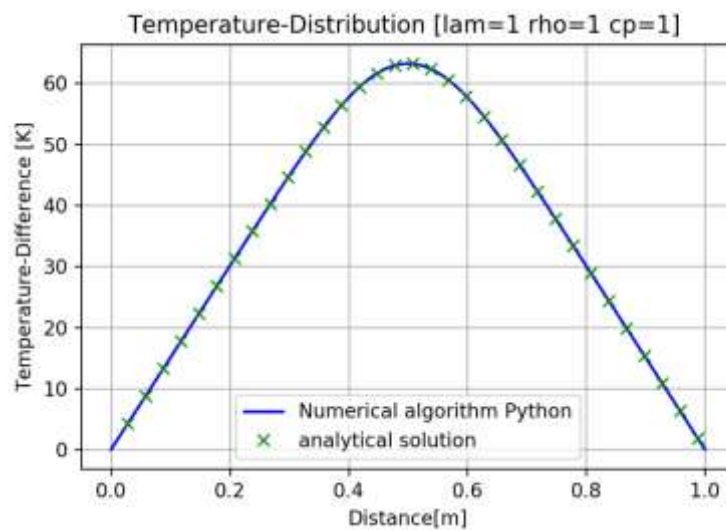


Figure 18: Comparison of the numerical Python® algorithm and the analytical solution [6]



## 7 Geometry & Mesh

As a simulation model represents a physical model, it is highly recommended to compare simulation results with an experimental data set. The following chapters will describe in brief:

- The setup of the simulation model (geometry and mesh) by using *ANSYS® Design Modeler* and the *ANSYS® Meshing Tool* of *ANSYS® Workbench*
- The method of importing the sensor-points into the simulation model
- Possibilities to reduce calculation effort by reducing the dimensions of the model

The process of geometry & mesh-generation in *ANSYS® Workbench* is performed independently to the simulation process, which is done with help of *ANSYS® Fluent*. It is recommended to generate several mesh files within the *ANSYS® Workbench*, while using *ANSYS® Fluent* in “stand-alone” mode. This leads to higher flexibility and simplifies data structures.

### 7.1 Geometry

Future investigations on changes of several geometric parameters such as the slope distance and the slope diameter allow to invest time in creating a parametrised geometry model at the beginning. This will save time in future, if thinking about changing parameters in course of later investigations. The geometry cell within the Workbench feeds other cells that provide data for the meshing tool (*Figure 20*). Following parameters can be adjusted inside the parameter cell (*Figure 19*):

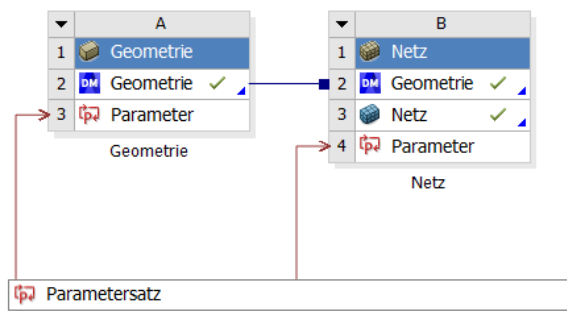


Figure 20: ANSYS® Workbench Structure

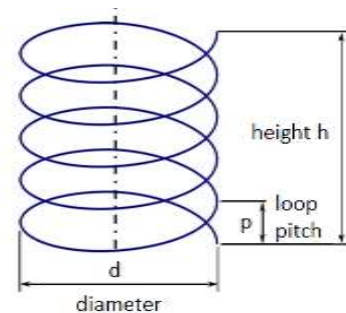


Figure 19: Parameters of the heating cable [19]

- The diameter ( $d$ ) of the helix
- The loop pitch ( $p$ ) of the helix
- The total height ( $h$ ) of the helix

In course of the project the goal is to test different helix configurations (loop pitch distances  $p$  and diameter  $d$ ) while keeping the location of the GHE inside the soil, constant.

The 3D - geometry model (Figure 21) inspired by the experimental setup (Figure 22) consists out of:

- A cubic box (Height= 1340 mm, Width= 720 mm, Length= 1115 mm)
- A heating cable in form of a helix (Height ( $h$ )= 1000 mm, Loop pitch ( $p$ )= 100 mm, Diameter ( $d$ )= 350 mm, cable diameter= 6 mm)

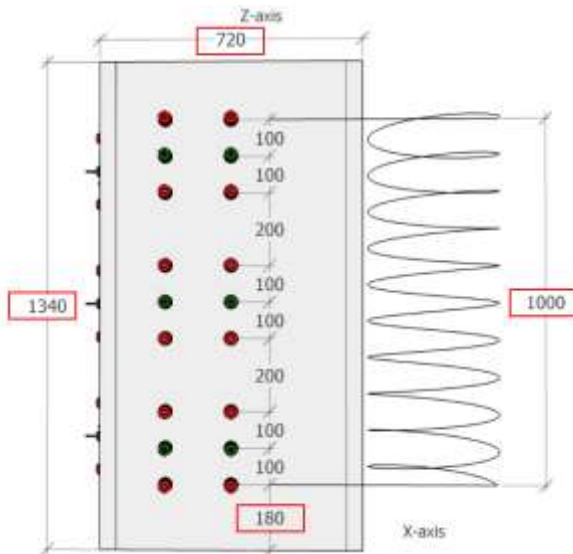


Figure 22: Dimensions of the box [19]

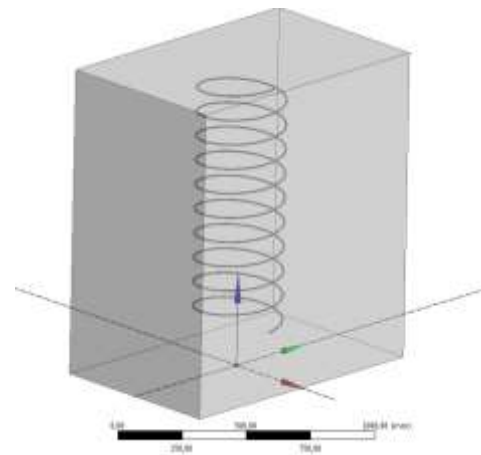


Figure 21: CFD Model

The coordinate system is located in the center of the box base (Figure 21).

While the starting point of the helix is located at  $(x,y,z) = (170 \text{ mm}, 0, 180 \text{ mm})$ , the end-point is at  $(x,y,z) = (175 \text{ mm}, 0, 1180 \text{ mm})$ .

The circle in the XZ – plane describing the cross section of the heating cable, is approximated by a polygon with  $n = 10$  edges. This helps the meshing algorithm to perform a stable and reproducible process of meshing.

## 7.2 Mesh

The convergence behaviour of the CFD simulation highly depends on the quality of the mesh used in the calculation. On one hand, important flow details are to be precisely recorded, on the other hand the computing times shall be acceptable. As fine as necessary, as coarse as possible is therefore the motto.

The 3D domain of the soil and the heat exchanger are displayed by help of a so called *unstructured mesh* which allows a very high degree of flexibility. The element shape used are

so called *tetrahedral cells (tet cells)*. One of the most important factors to check the quality of the mesh is the skewness. It can be shown that a too high skewness leads to instabilities and lower accuracy. For practical applications it is recommended that the skewness factor does not exceed 0.9.

In terms of generating the mesh on the base of the geometry, following rough references are given, based on practical experiences. This information helps to keep the calculation effort within economical boundaries:

- Maximum number of ten equilateral triangles to describe the circle of the heating cable in the XZ- plane
- Better resolution near the helix than in boundary regions of the box because of the temperature gradient being expected
- Wall-boundary cells may be bigger sized within limits of 50 to 100mm per cell
- As a rough estimation the number of cells should not exceed one million

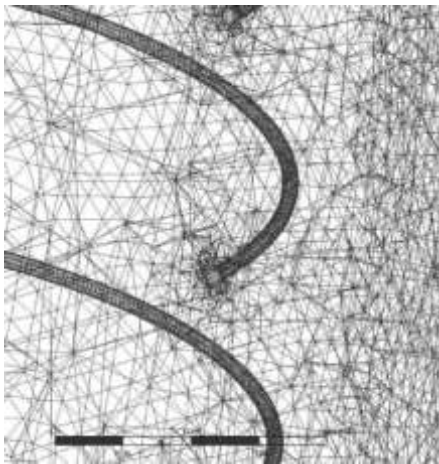


Figure 24: Mesh on the heating cable

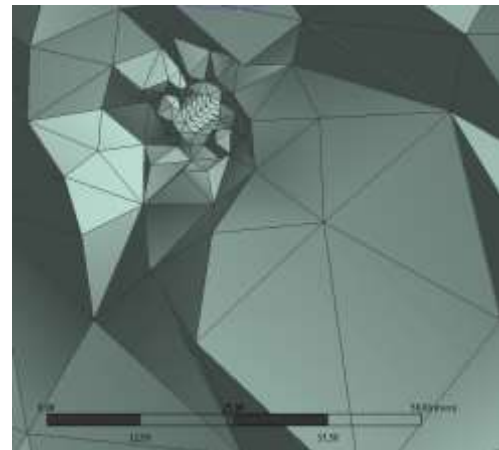


Figure 23: Mesh refinement and growth factor

These requirements suggest the application of a growth factor, starting with small elements on the helix with increasing element size towards the walls. Different growth rates are tested to show the (in)dependence of simulation results and growth rate. As smaller growth-rate leads to a significantly higher number of elements. Therefore a good compromise between accuracy and calculation effort has to be chosen.

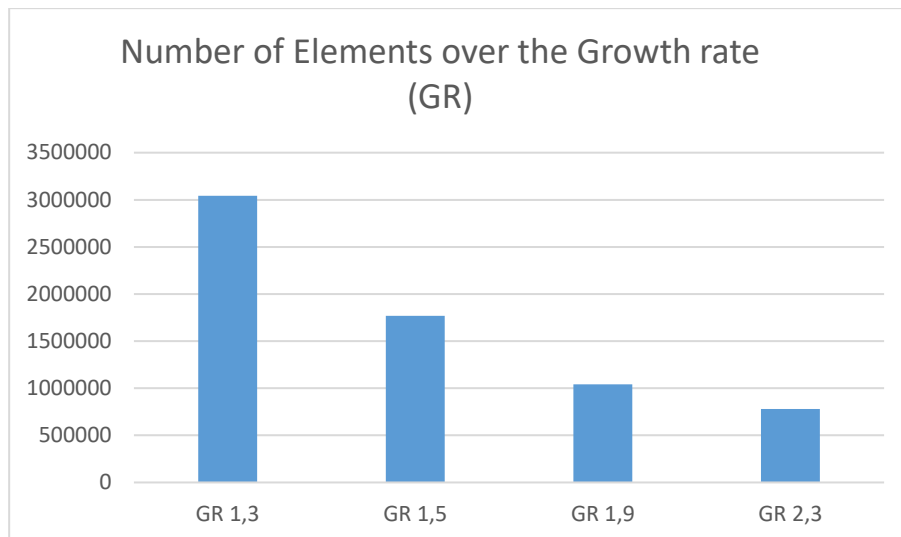


Figure 25: Number of elements over the growth rate (GR)

Furthermore local mesh-refinement on specific points in the mesh is performed to reduce a potential dependency of the numeric solution regarding element size.

The 3D-mesh consists out of tetrahedron elements while surfaces are meshed by help of triangle elements. The mesh has the following important element characteristics:

- Elementsize (Wall\_box\_length1) = 50mm
- Elementsize (Wall\_box\_length2) = 50mm
- Elementsize (Wall\_box\_width1) = 50mm
- Elementsize (Wall\_box\_width2) = 50mm
- Elementsize(Wall\_box\_top) = 30mm
- Elementsize(Wall\_box\_bottom) = 30mm
- Elementsize(Wall\_heatingcable\_middle) = 1.85mm

As element size is getting greater from small sized elements on the heating cable (Wall\_heatingcable\_middle) to the walls of the cubic box. The following growth rate is implemented into ANSYS® due to a good compromise between accuracy and calculation effort:

- Growth rate = 1.9 → Number of elements = 1 041 740

### 7.3 Implementation of the Sensorpoints

A validation asks for a comparison of experimental sensorpoint-values with calculated physical values on these points in the simulation domain. Therefore, the location of the fibre optics sensors have to be imported into the simulation model. This is performed by defining a particular helix after following parametrisation in cartesian coordinates:

$$\vec{x}(t) = \begin{pmatrix} r * \cos(2\pi t) \\ r * \sin(2\pi t) \\ h * t + c \end{pmatrix} \quad (50)$$

- While  $t \in R$  is known as the number of the windings starting at the point  $\vec{x}(0)$
- $h$  is known as the slope distance. It is the distance that is covered by a full turn
- While  $r$  is the radius of the helix,  $c$  represents the offset of the helix in z-direction

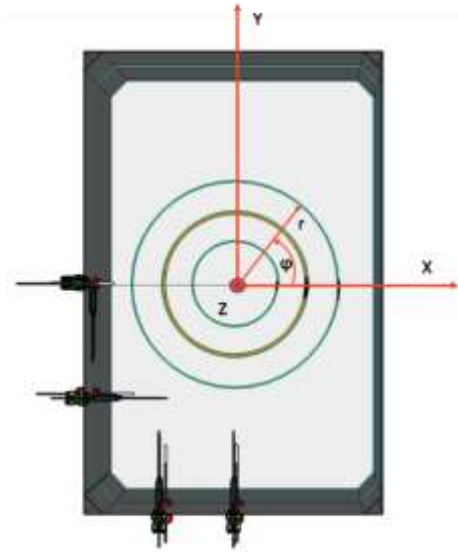


Figure 26: Polar coordinate system to describe the sensorpoint location [19]

The coordinates of the sensorpoints are generated in *EXCEL*®. A *Python*® program helps to create a data structure that is afterwards converted into a *.txt* file which can be imported into *ANSYS*® *Fluent* in form of a journal file. This journal file contains code-instructions to import the sensorpoints automatically. *Table 4* in the appendix gives an overview of the sensorpoints location on the fibre optics cable.

The sensorpoint positions are split into three main categories which are highlighted in different colours. This is done as follows:

- Inner (blue)
- Middle (orange)
- Outer (green)

The incremental step size  $\Delta t$  that is needed to transform the Polar coordinates of the fibreoptic coils into Cartesian coordinates is dependent on the sensorpoint-locations on the fibreoptics cable. Important fact to be mentioned is, that  $\Delta t$  must not be seen in context to time in that case. As the fibreoptics cable has a resolution of  $n=1$  sensorpoint per length=0.5m, resolution was doubled by using two coils of fibreoptics within the same basket. This leads to a final

resolution of  $n= 1$  sensorpoint per length= 0.25m. The incremental step size  $\Delta t$  can be calculated as follows:

$$\Delta t = \frac{\text{Distance between the sensorpoints on the fiberoptics cable [mm]}}{\text{circumference of the fiberoptics coil [mm]}} \quad (51)$$

$$t_{n+1} = t_n + \Delta t \quad (52)$$

Figure27 gives an overview of the implemented sensor points inside the domain.

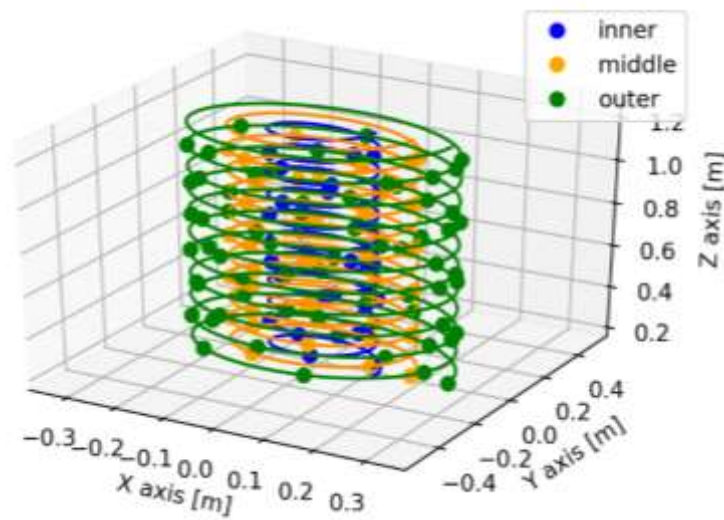


Figure 27: 3D Plot of the sensorpoint location [21]

## 7.4 Boundary Conditions

Boundary conditions were set to following constant values:

- $T_w = 283.15K$  (valid for all box walls)
- $\dot{q} = 553.63 \text{ W/m}^2$  ( $113.1\text{W}/0.204\text{m}^2$ )

## 7.5 Soil characterization

The simulation is set up in *ANSYS® Fluent* by using temperature dependent material properties given by thermophysical laboratory testing performed at AIT. To get a quick overview

on the value size of each parameter, *Figure62&63* in the appendix shows the values at a temperature of  $T=20^{\circ}\text{C}$ .

To guarantee the correct implementation of the material data in the simulation, the thermal properties and their temperature dependence ( $\lambda(T)$ ,  $\rho$  and  $c_p(T)$ ) must be analysed with an appropriate measuring method. This is done with help of the Heat-Flow-Meter (HFM) measuring method which is standardized according to *DIN EN 12664/12667* and *ASTM C 518*. Density is assumed to be independent of the temperature and tested to be  $\rho=1822\text{ kg/m}^3$ . The first experimental tests are carried out in the thermophysics laboratory of AIT using "dry sand" as the soil medium. Results and calculated uncertainties are given in the appendix.

## 7.6 Simplification into 2D space

As a 3D simulation domain with adequate mesh resolution requires a huge computational effort, a concept is created to reduce calculation time. This goes hand in hand with speeding up the process of knowledge gaining.

The idea is to create a 2D model, which simplifies the 3D-helix. A hollow cylinder with infinite height in  $Z$  dimension and same thickness as the copper heating cable serves as approximation.

*Figure28* shows the mesh of the 2D cylinder model including the naming and colouring of the fiberoptic-cables. The visualization of the results in several diagrams is performed in this colours.

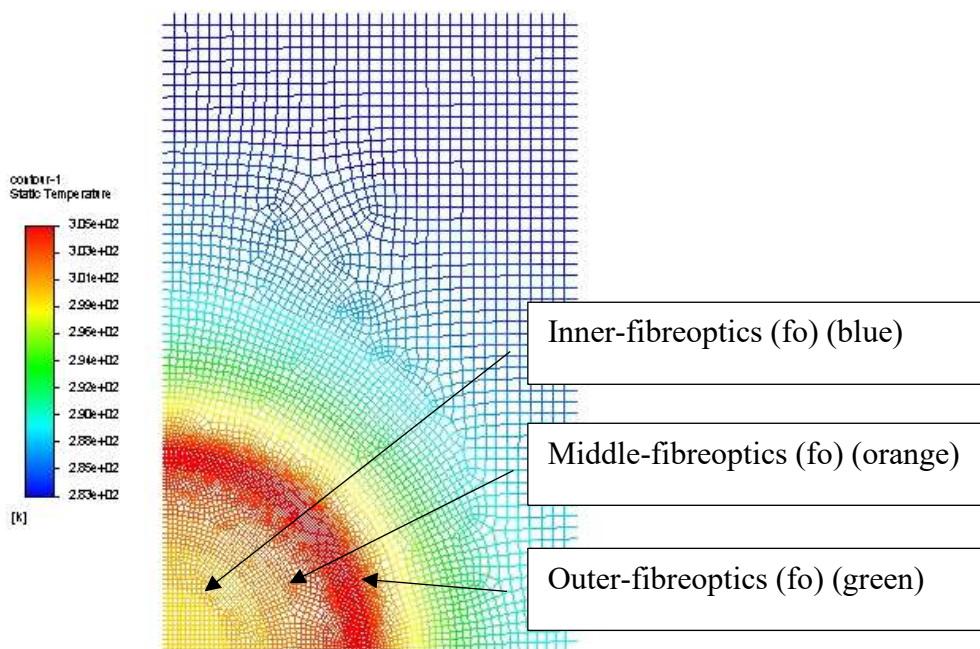


*Figure 28: Temperature distribution of the 2D Cylinder Model*

## 8 Comparison of experiment and simulation

In this chapter simulation and experimental data are compared in 3D-space.

### 8.1 Experiment

Figure 29 shows the experimental temperature-levels of the inner- (blue), middle- (orange) and outer-fibreoptics-cable (green) after a time of  $t+0h$ ,  $t+8h$ ,  $t+16h$  and  $t+24h$ .

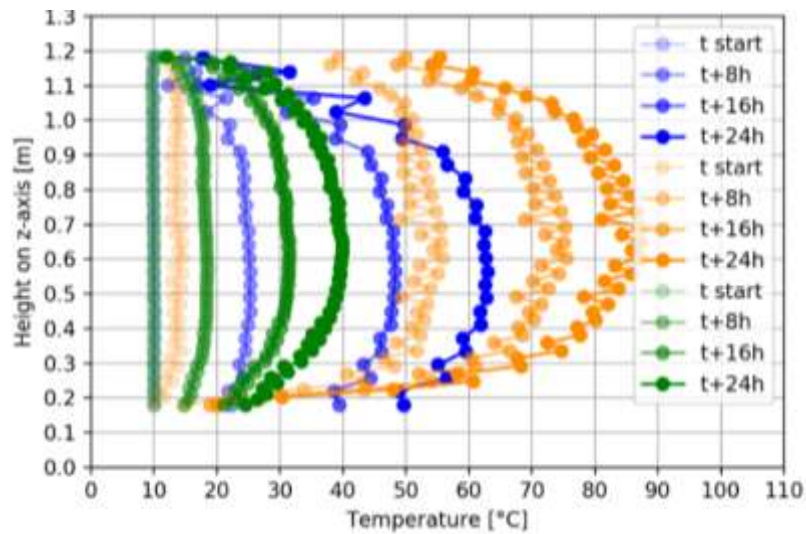


Figure 29: Height in Z over temperature T of the experimental data [21]

Figure 29 shows the heights on z-axis [m] over the temperature levels T reached in the box. Following experimental temperatures  $T_{exp}$  are reached in the center of the box:

- $T_{exp}$  (inner/t+24h\_exp) = 62.1°C
- $T_{exp}$  (middle/ t+24h\_exp) = 87.2°C
- $T_{exp}$  (outer/ t+24h\_exp) = 40.0°C

The experimental curve of *Inner-fibreoptics* shows asymmetric characteristics along the horizontal symmetry axis compared to other measurement spirals. Possible reason might be inhomogeneous boundary conditions as the cooling fan inside the cooling chamber is generating an additional *forced convection* at the top.



## 8.2 Simulation vs. Experiment

Figure 30 shows the experimental data-set compared to the simulation data using the 3D simulation model.

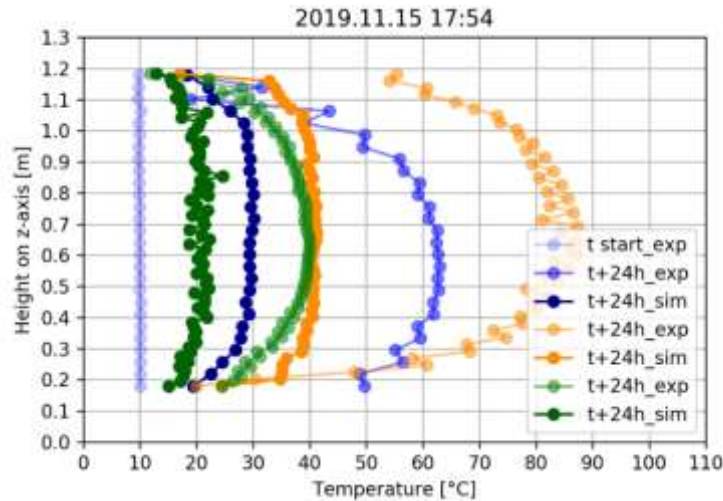


Figure 30: Comparison of simulation and experiment @  $t+24h$

Figure 30 shows, that the temperature levels of the simulation are far too low. Following temperatures are reached, while the ratio between  $T_{exp}$  and simulation  $T_{sim}$  are shown on the right:

- $T_{sim}(\text{inner}/t+24h\_sim) = 29.8^{\circ}\text{C}$   $\frac{T_{exp}}{T_{sim}} = 2.1$
- $T_{sim}(\text{middle}/ t+24h\_sim) = 41.1^{\circ}\text{C}$   $\frac{T_{exp}}{T_{sim}} = 2.1$
- $T_{sim}(\text{outer}/ t+24h\_sim) = 21.4^{\circ}\text{C}$   $\frac{T_{exp}}{T_{sim}} = 1.9$

The simulation curve of *outer-fibreoptics* is not that “smooth” compared to experimental data. Possible reason could be found in the “rougher” boundary conditions of the simulation compared to experimental ones. This might lead to a greater influence on outer areas.

Temperature levels of the experiment are by far greater than the calculated results. The highest deviation of  $T_{exp}$  compared to  $T_{sim}$  could be found on the fibreoptics-cable in the middle (orange).

## 9 Parameter Variation

A parameter variation will provide results to gain a better understanding of the physical principles behind the process of heat exchange. As temperature levels of experiment and simulation show huge differences (see chapter 8) parameter variation will help to gain a better understanding of the heat transfer process. Following variations are performed:

- Time-Step Variation (to speed up the simulation process)
- Local mesh refinement
- Variation of the thermal diffusivity  $a$  in 2D
- Variation of the thermal diffusivity  $a$  in 1D
- Variation of the density  $\rho$
- Variation of the heat transfer coefficient  $\alpha$
- Variation of the power input  $P$

### 9.1 Time-Step Variation

One goal is to reduce the calculation effort to a minimum, to guarantee efficiency. It is important to check, if the time-step size has an influence on the output of the simulation. In this simulation series, the influence of the time-step size is checked by doing transient simulations with following time-step sizes:

- 10 [s]
- 100 [s]
- 1 000 [s]
- 10 000 [s]

Following plots show the temperature of the Middle-basket over time. The data of different time-steps are overlaid in these plots. The different plots (*Figure31-33*) compare the time-steps 100s, 1000s and 10000s to the smallest time-step of 10s. The solution using a time-step size of 10s shows best accuracy and is indicated as a continuous graph.

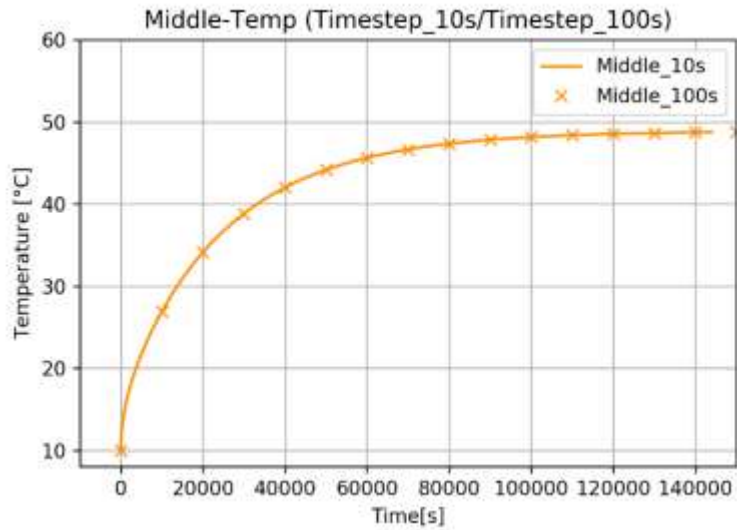


Figure 31: Comparison of time-step 10s and time-step 100s

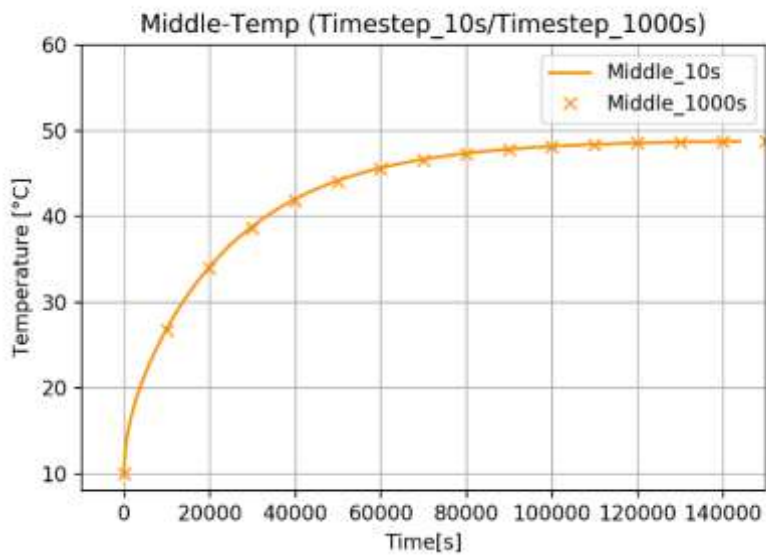


Figure 32: Comparison of time-step 10s to time-step 1000s

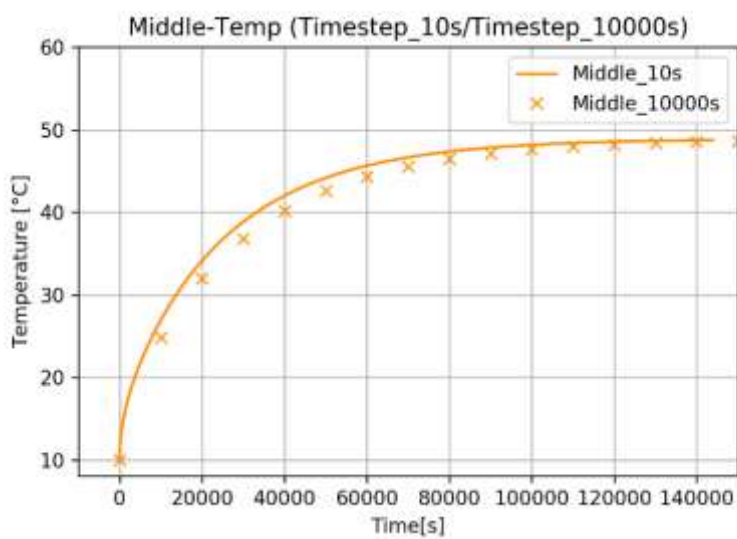


Figure 33: Comparison of time-step 10s to time-step 10000s

*Figur32* and *Figure33* show a good fit of the graphs. The transient (time-dependent) part of the solution shown in *Figure34* shows a deviation of the values, while steady state solution is unaffected by the increase of the timestep-size.

As the simulation with a timestep-size of 1000s shows good accuracy while reducing calculation effort by a factor of approximately 100, the higher time-step size is chosen. This guarantees significantly faster results with less effort while precision of the solution is given.

## 9.2 Local mesh-refinement

A CFD calculation solves the heat equation on specific points in the domain. The “correct” values of the temperature field  $T$  are calculated in the center of the tetrahedral-elements. When comparing simulation to experimental data on given locations, which do not match cell centers, approximations are needed. The approximation error of the calculated result is, as a result, depending on the size of the elements. For that reason it is necessary to perform a local mesh refinement to compare results of the refined mesh with results of the original one.

The local mesh refinement is performed at specific points in the mesh (i13, m23 and o33), which are representing experimental sensor points on each basket. The location of the specific points can be found in the appendix.

Characteristics of the Sphere of Influence (SOI):

- SOI5: SOI diameter: 5 mm, element-size: 0,5mm, Timstep= 1000 s
- SOI100: SOI diameter: 100 mm, element-size: 10mm, Timstep 1000 s

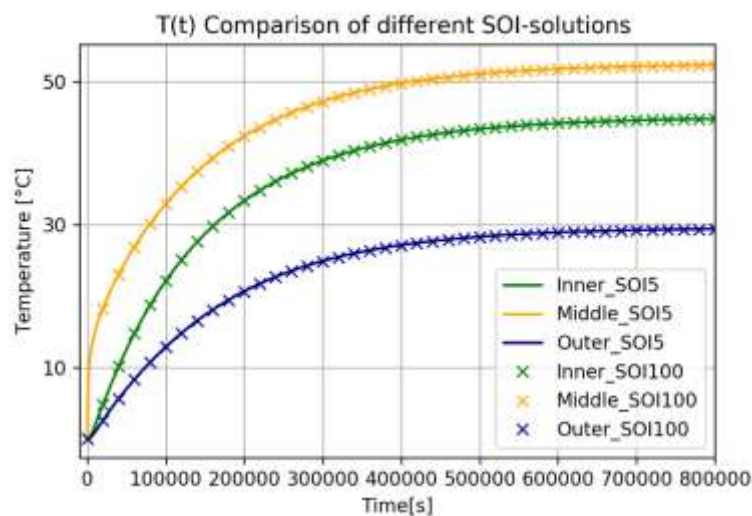


Figure 34: Comparison of SOI5 and SOI100

Figure 34 shows a comparison of *SOI5* and *SOI100*. To guarantee better visibility *SOI100* is shown in a lower resolution. The graphs match in a good manner, which indicates that calculation results on the specific points are equal and not depending on the element size in a range of 0.5mm and 10mm.

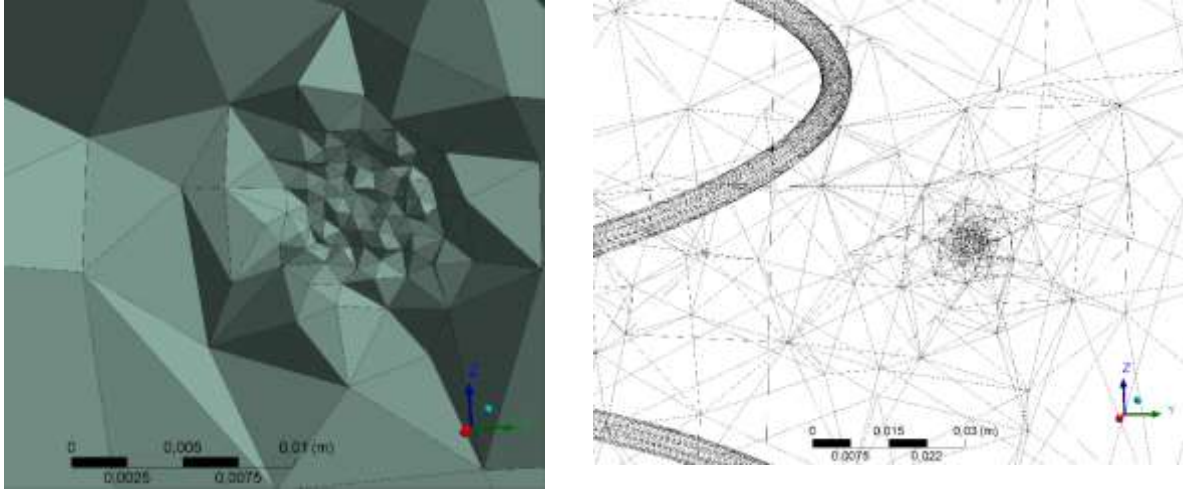


Figure 35: Local mesh refinement of sensorpoint o33 with *SOI5*

It can be said that element sizes ranging from 0.5mm to 10mm on specific selected sensorpoints do not result in a change of temperature levels  $T$  in the simulation. The solution is independent of the grid size in that range.

### 9.3 Variation of $a$ in 2D

The *thermal diffusivity*  $a$  is clearly defined by following material parameters:

- The thermal conductivity  $\lambda$
- The specific heat capacity  $c_p$
- The density of the material  $\rho$

The combination of these parameters can be interpreted as a single coefficient  $a$  (thermal diffusivity) which defines the characteristic of the  $T(t)$  curve. A basic parameter set is defined as follows:

$$\lambda = 0.4 \frac{W}{mK}, c_p = 900 \frac{J}{kgK}, \rho = 1800 \frac{kg}{m^3}$$

A combination of these parameters doubled or halved will allow relative statements. The setting of the parameters [in SI-units] is as follows:

Variation of thermal soil-properties				
	$\lambda$ [ $\text{W m}^{-1} \text{K}^{-1}$ ]	$c_p$ [ $\text{J kg}^{-1} \text{K}^{-1}$ ]	$\rho$ [ $\text{kg m}^{-3}$ ]	relative combination
Test1	0.4	900	1800	(1,1,1)
Test2	0.8	900	3600	(2,1,2)
Test3	0.8	1800	1800	(2,2,1)
Test4	0.4	3600	3600	(1,1/2,2)
Test5	0.4	1800	1800	(1,2,1)

Table 1: Variation of thermal soil-properties in 2D

Figure36 shows the result of this material property variation. It can also be interpreted as a variation in thermal diffusivity. The vertical dashed black line indicates  $t+24h$ .

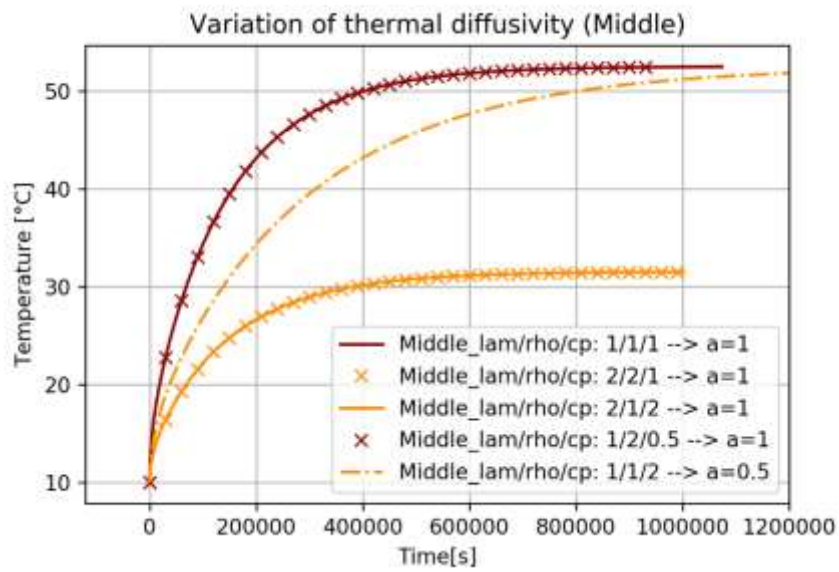


Figure 36: Variation of different thermal diffusivities a

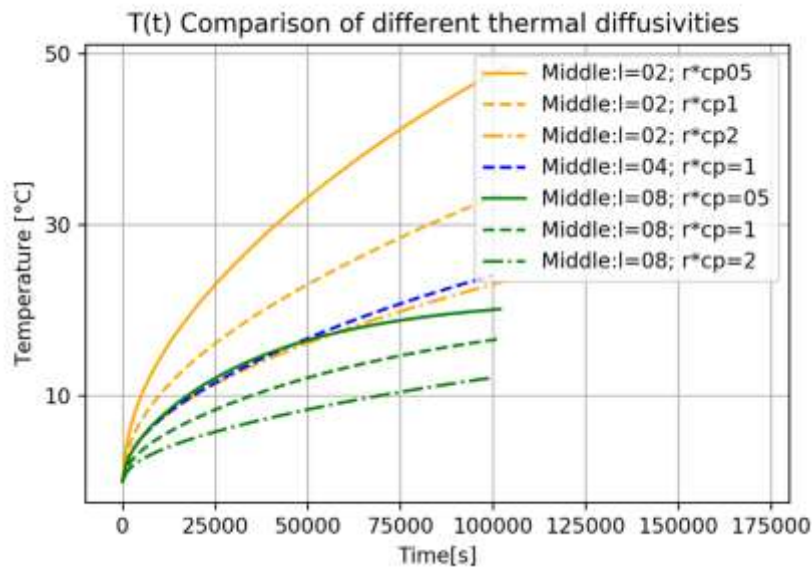


Figure 37: Comparison of different thermal diffusivities

While *Test1* and *Test4* fit together, *Test2* and *Test3* match together. *Test5* reaches steady state “slower” while the temperature levels are equally to *Test4* and *Test1*.

The temperature level of the long-term solution (steady state solution) is affected by the thermal conductivity  $\lambda$  only. The lower the thermal conductivity  $\lambda$  is, the higher temperatures are, that can be reached in steady state.

If the denominator value of the *thermal diffusivity*  $a$ , which is the product of  $(\rho \cdot c_p)$  is increasing, while  $\lambda = \text{const.}$ , the time to reach steady state increases as well. In other words: The product of the materials density  $\rho$  and the specific heat capacity  $c_p$  provide information about the transient part of the differential equation only, while  $\lambda$  provides information about the steady state solution.

#### 9.4 Variation of $a$ in 1D

To confirm the effects shown in the chapter before, a parameter variation of the 1D rod model is shown. Parameter setting are defined as follows:

Variation of normalised thermal soil-properties				
	$\lambda$ [-]	$\rho$ [-]	$c_p$ [-]	$a$
<i>Simulation 1 (red)</i>	1	1	1	1
<i>Simulation 2 (blue)</i>	1/2	1	1	1/2
<i>Simulation 3 (green)</i>	1	1	1/2	2

Table 2: Variation of normalised thermal soil-properties in 1D

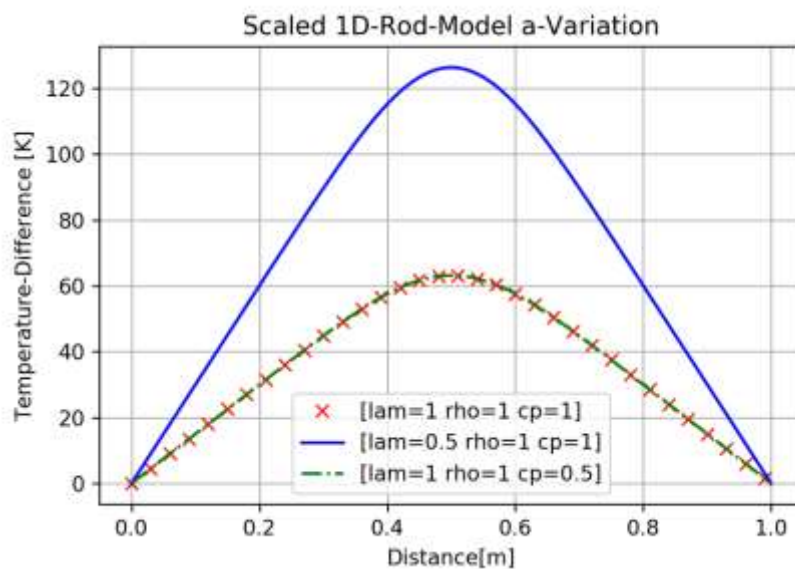


Figure 38: Variation of the thermal diffusivity on the scaled 1D rod model

The lower the thermal conductivity  $\lambda$ , the higher temperatures levels in steady state can be. The steady state solution of the temperature distribution is not affected by the combination of  $\rho \cdot c_p$  in the denominator of the thermal diffusivity. The 2D cylinder model and the 1D rod model show conform behaviour.

### 9.5 Variation of the density $\rho$

This simulation series shows the “speed-up” of the transient part of the differential equation. It is executed with  $\lambda_{\min}$ ,  $c_{p\min}$  while  $\rho$  is varying from the tolerance minimum of the laboratory test ( $\rho_{\min}$ ), reducing it afterwards to  $822 \frac{kg}{m^3}$ . The black vertical line represents a time of  $t+24h$ .

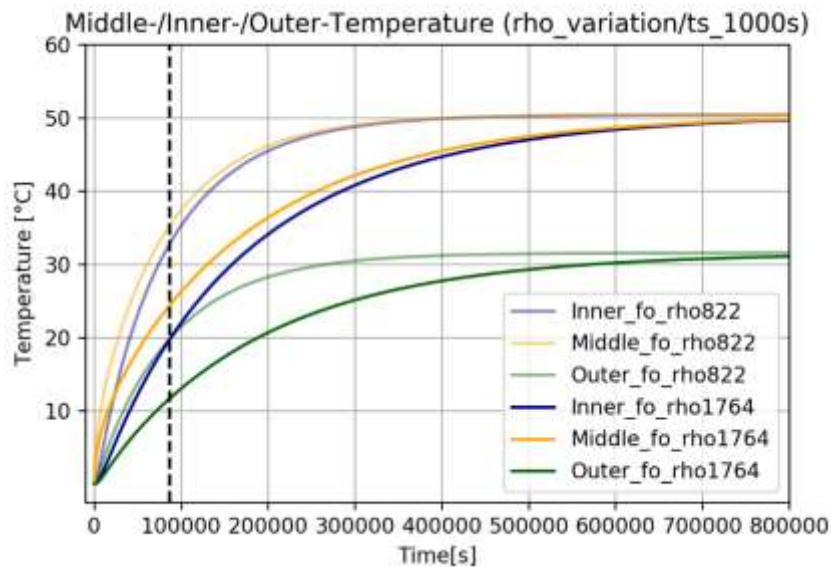


Figure 39: Variation of the density  $\rho$

While keeping  $\lambda$  and  $c_p$  to a constant minimum, which is defined by the lower limit of the statistical material characterization boundary,  $\rho$  reduction shows, that temperature levels are reached faster.



## 9.6 Variation of the heat transfer coefficient $\alpha$

As the characteristic of the temperature field  $T(x,y,z,t)$  inside of the box is also affected by the *Boundary Conditions*, sensitivity of the simulation result on  $\alpha$ -changes have to be checked. In this test series, the influence of *forced convection* on the systems boundaries is tested by comparing a heat transfer rate of  $\alpha=1$  to a heat transfer rate of  $\alpha=10$  [ $\text{W m}^{-2} \text{K}^{-1}$ ].

Practically, forced convection can be added to the system by help of a fan for example. As the cooling chamber is cooled by fan, this is indeed the case. Physically increasing  $\alpha$  can be seen as follows:

*If  $\alpha \rightarrow \infty$ , the BC's can be interpreted as a fixed temperature.*

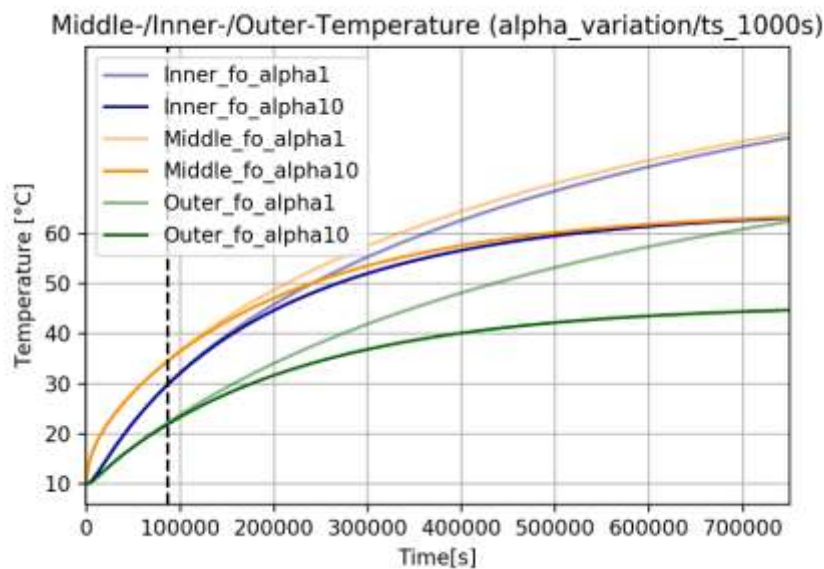


Figure 40: Temperature of different heat transfer coefficients on  $T-t$

The temperature levels of *Inner/Middle/Outer* with *alpha1* and *alpha10* match perfectly for times up to  $t=24\text{h}$ . While simulation continues, temperatures-difference between *alpha1* and *alpha10* is increasing as well. The steady state solution is reached faster, the higher  $\alpha$  is.

The higher the transfer coefficient  $\alpha$  gets, the “harder” the BCs get. Setting the boundaries to constant temperature of  $T=283.15\text{K}$  is a really “hard” boundary condition, which can only be reached by using a fluid (high  $\alpha$ ) that is cooling the walls of the box walls for example. Hard boundary conditions result in a steady state that is reached faster.

## 9.7 Variation of the Power input

Temperature levels (steady state) could either be raised by decreasing the thermal conductivity  $\lambda$  or by increasing the Power input injected/extracted into the surrounding ground. A simulation series with increased Power input will show this influence. As the cylinder model does not show a temperature distribution over z-axis, another simulation is performed to present effects in 3D space.

### 9.7.1 2D cylinder model

The form of the differential heat equation implies, that the temperatures inside the box can also be increased by increasing the power input.

The power input is increased until *middle-fibreoptics* reaches approximately the temperature levels of the experimental data after  $t+24h$ .

*Figure41* shows the temperature over time of *inner-/middle-/outer-fibreoptics*. The black vertical line represents a timestamp of  $t+24h$ .

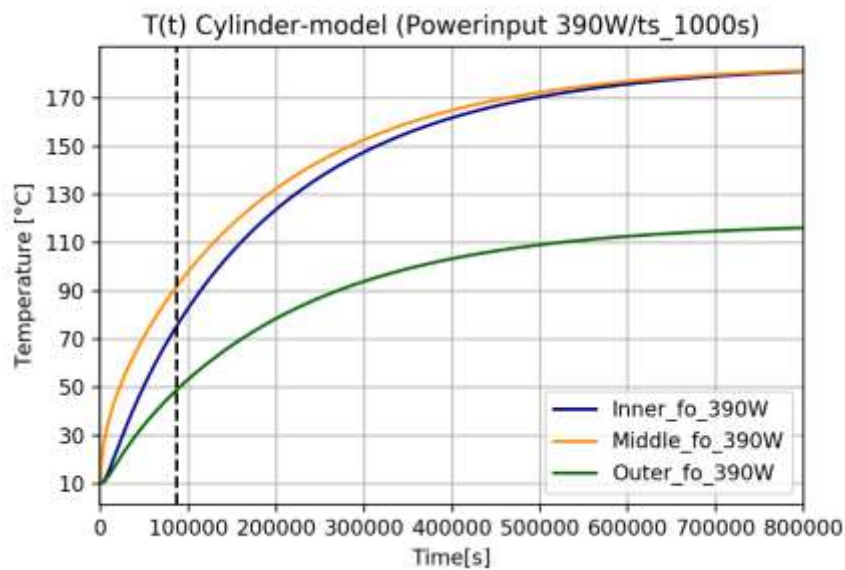


Figure 41: Power input of 390W into the cylinder model

Following temperatures are reached after  $t=24h$  of simulation

- $T(\text{inner\_fo}/t+24h) = 73^{\circ}\text{C}$
- $T(\text{middle\_fo}/t+24h) = 90^{\circ}\text{C}$
- $T(\text{outer\_fo}/t+24h) = 50^{\circ}\text{C}$

By interpreting the material properties as given, the power input must be increased to about 390W to reach approximately the same temperature levels on the middle-fibreoptics compared to the experimental data set. The steady state solution reaches very high temperatures up to 180°C. The measurement system and the heating cable would suffer damage in case of reaching steady state solution.

### 9.7.2 3D helix model

Figure 42 below shows a temperature comparison of 3D simulation and experiment after a time of  $t+24h$ . The Power input is set to  $P=280W$ .

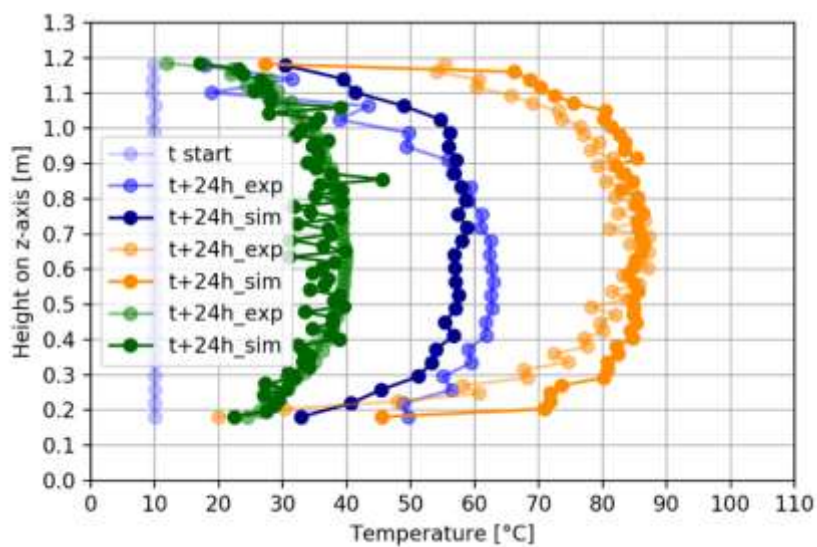


Figure 42: Temperature Comparison of 3D Simulation and Experiment @ $t+24h$  (Power-input= 280W)

The curve of the simulation data of outer-fibreoptics (green) is not that smooth compared to the experimental data set. The volatile behaviour of the *outer fibreoptics* could possibly be influenced by the “harder” boundary conditions in the simulation. As the temperature is set to  $T=const.$  this could be interpreted as a very high heat transfer coefficient (box in water f.e.).

The *inner* data set of the experiment shows asymmetric from while the simulation data set is symmetric. The asymmetry of the inner curve in the experiment could be caused by inhomogeneous boundary conditions (fan on top side, no convection on bottom).

To match the temperature levels of the sensorpoint *m23* (see Table 3) a power input of  $P=280W$  is needed.

Temperature comparison @t+24h		Inner (i13)	Middle (m23)	Outer (o33)
P = 113W	T <sub>exp</sub> [°C]	62.1	87.2	40.0
	T <sub>sim</sub> [°C]	29.8	41.1	21.4
	ΔT [°C]	32.3	46.1	18.6
	T <sub>exp</sub> /T <sub>sim</sub> [-]	2.1	2.1	1.9
P = 280W	T <sub>sim</sub> [°C]	58.1	86.0	37.6
	ΔT [°C]	4	1.2	2.4
	T <sub>exp</sub> /T <sub>sim</sub> [-]	1.1	1.0	1.1

Table 3: Temperature comparison @ t+24h

The temperature distribution in the earth basket with a power input of P= 280W shows a good agreement at the middle fibre optic cable of  $\frac{T_{exp}}{T_{sim}} = 1.0$ , while small deviations of  $\frac{T_{exp}}{T_{sim}} = 1.1$  on outer and inner must be mentioned.

Further research work performed at AIT finally showed that the disagreement of simulation and experiment truly had their origin in a wrong power measurement system. Results of this work are illustrated in the master's thesis of DI Constantin Doerr [6]. *Figure43* shows a comparison of the simulated and experimental steady state solution by using the correct power measurement system.

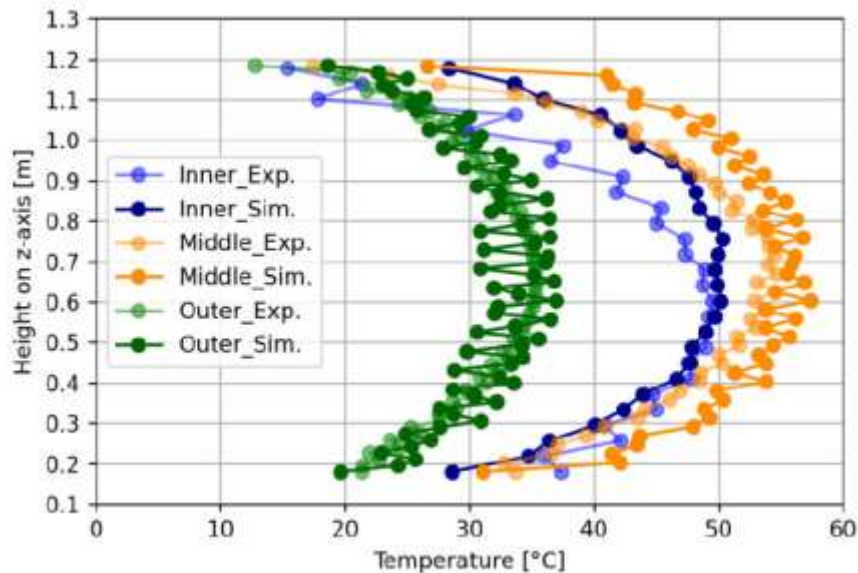


Figure 43: Simulation and experiment results from fibre-optic temperature sensors at steady-state [6]

## 9.8 Comparison of the 2D-cylinder model and the 3D-helix model

This test shows a comparison of the simplified 2D cylinder model and the 3D helix model. Results are shown in *Figure44*.

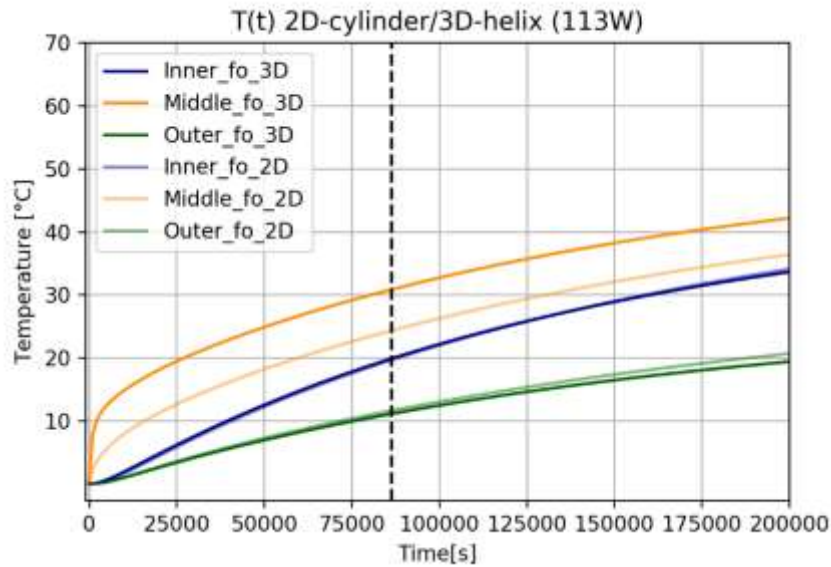


Figure 44: Comparison of 2D cylinder model and 3D helix model

*Inner-* and *outer fibreoptics* (green and blue) show a good match within the first 24h of simulated time.

*Middle fibreoptics* of the 3D model show higher temperature levels compared to levels of the 2D model. As the spiral pipe sections of the GHE interfere in z-direction (3D-model), possible reason for this phenomenon could be seen in an early thermal saturation along the z-axis of the box. This saturation could have effects onto heat exchange, resulting in higher temperatures T.

## 10 EURECAT/ global field simulation

One overall goal of GEOFIT is to show global field simulation results that can be used for future building simulations in different European climate zones.

To create a simulation tool in a large scale, data is provided by the simulation of one single earth basket. It is important to define the interface of the single earth basket simulation and the global field simulation clearly. The temperature data  $T$  and heatflux data  $\dot{q}$  provided by AIT will be further processed and implemented into a global field simulation by the Spanish research institute EURECAT. Temperature data  $T$  and heatflux data  $\dot{q}$  are exported on the walls of a cylinder that is implemented into the existing model.

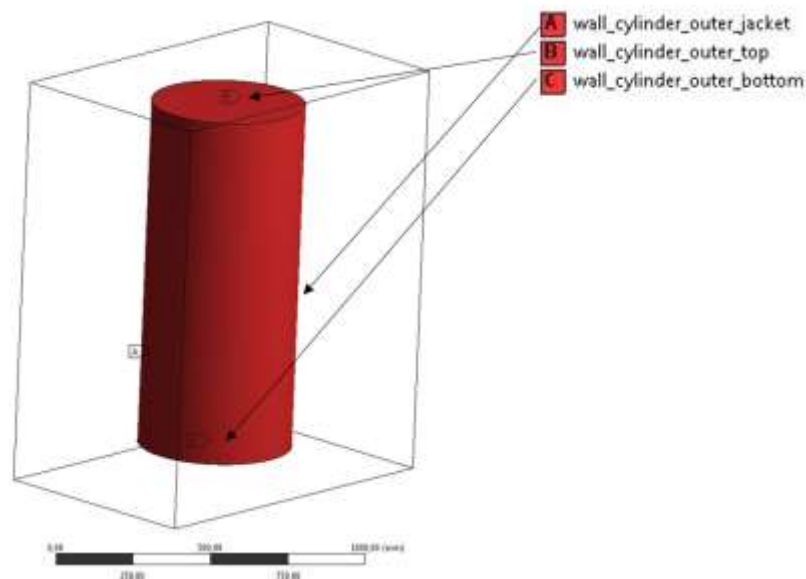


Figure 45: Eurecat cylinder model

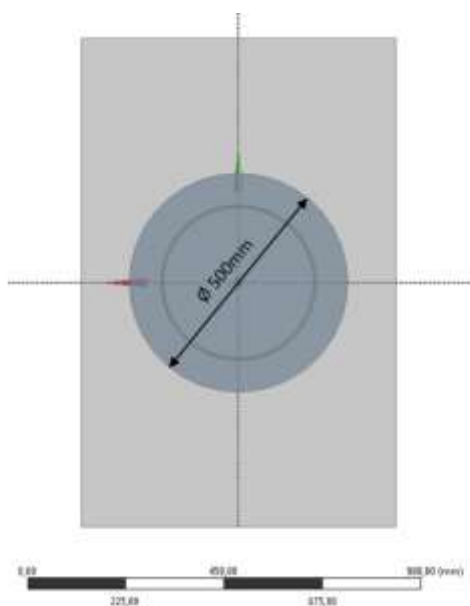


Figure 46: Diameter of the cylinder inside the box

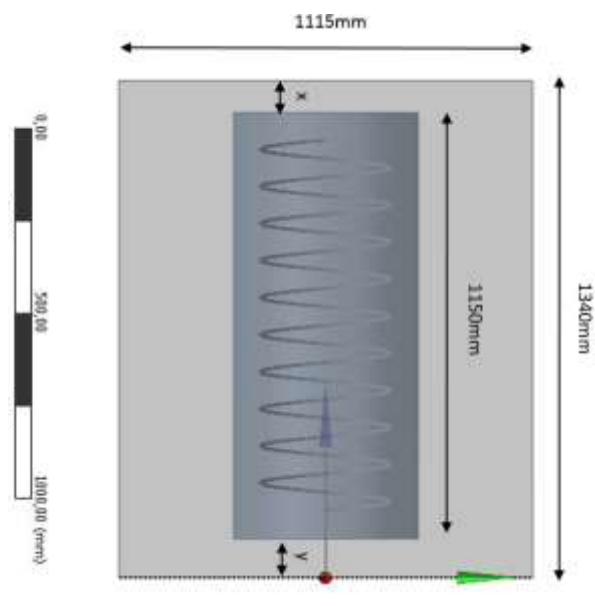


Figure 47: Position of the implemented cylinder in the box ( $X= 85\text{mm}$  and  $Y= 105\text{mm}$ )

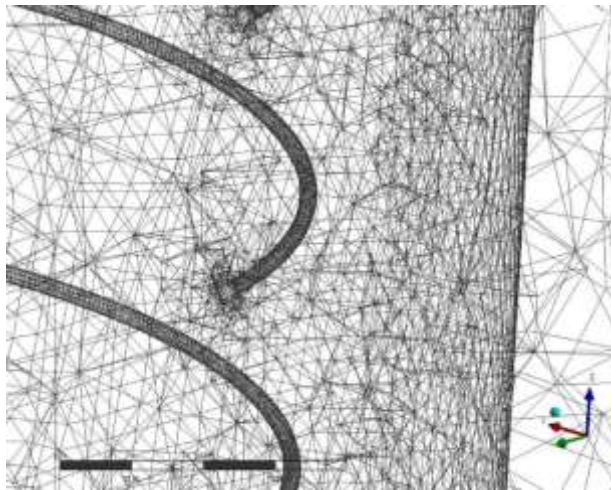


Figure 49: Mesh refinement on the heating cable

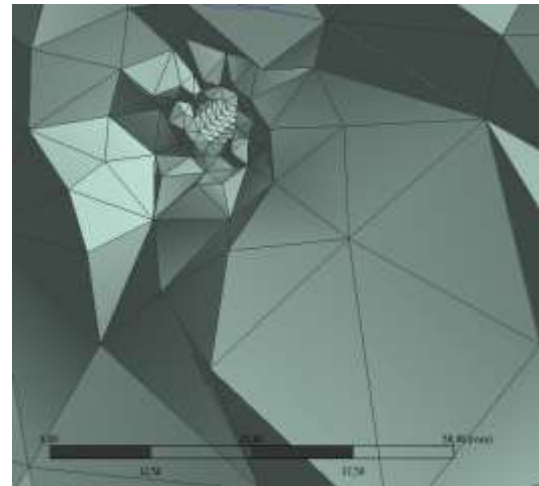


Figure 48: Mesh refinement and growth rate

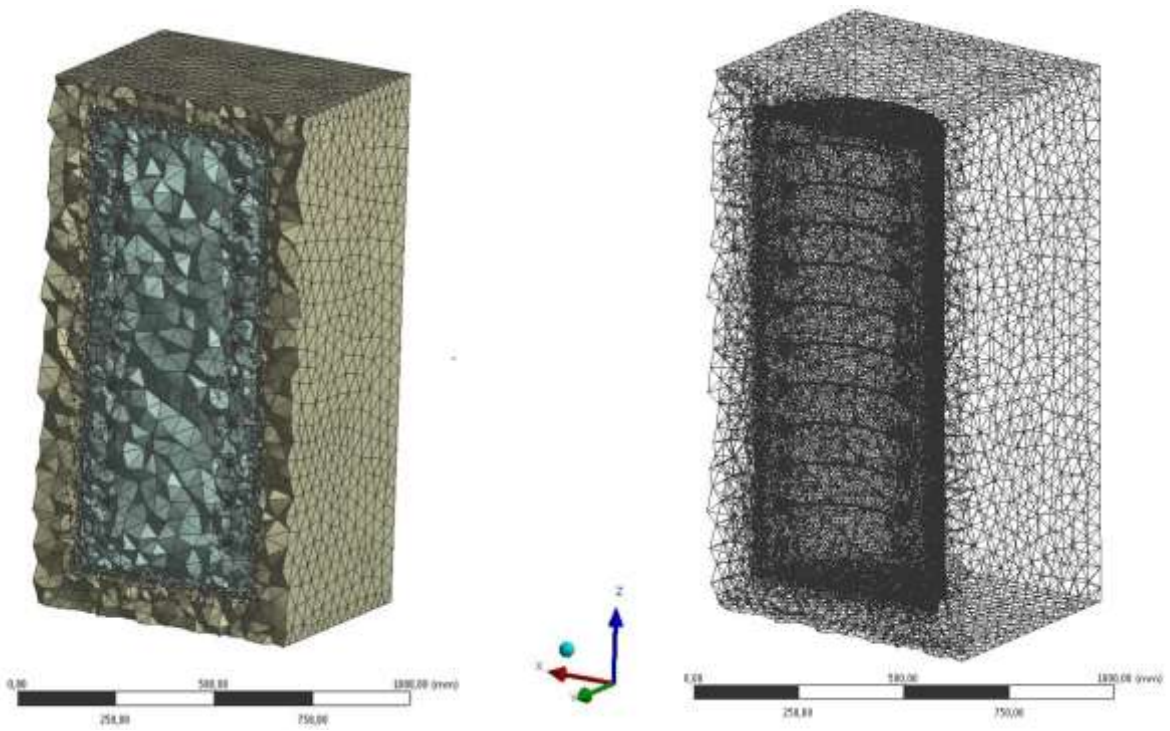


Figure 50: Grid view of the 3D Mesh model (left) and zoom onto the heating cable mesh (right)

The dataset that is given to Eurecat, is shown in green. Middle and Inner are additional curves to show tendencies on the heating cable (middle) and the inner fibreoptics. The diagram shows a Single Point Comparison at inner (i13), middle (m23) & outer (o33) fibre-optics with points at following coordinates:

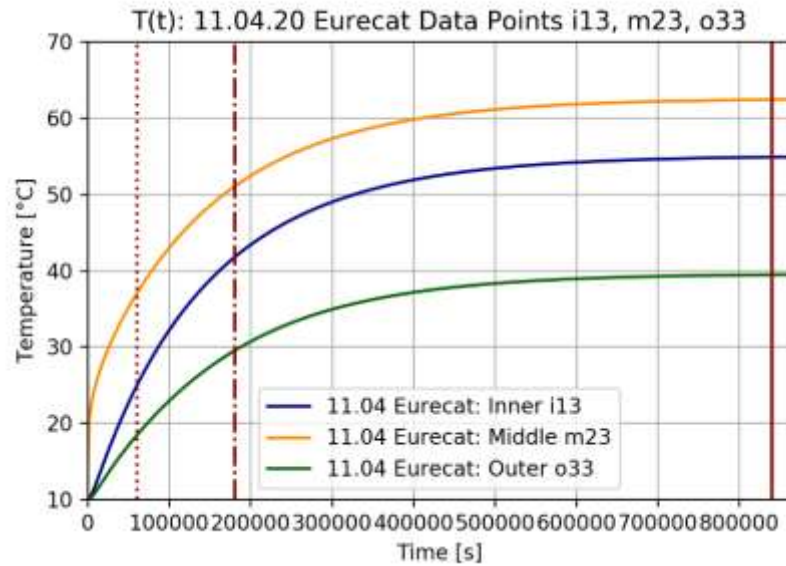


Figure 51: Single Point Comparison @timestep 60, 180, 840 (Timestep size 1000s)

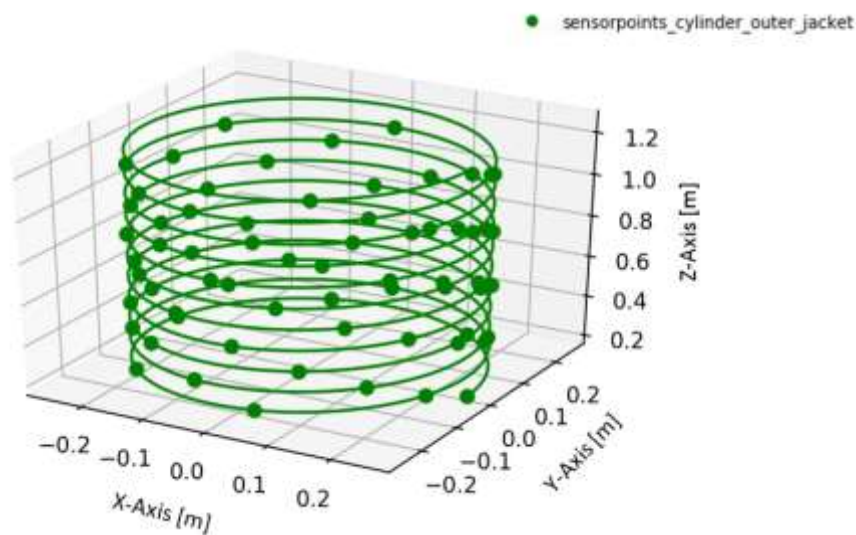


Figure 52: Fibreoptics sensorpoints on cylinder\_outer\_jacket



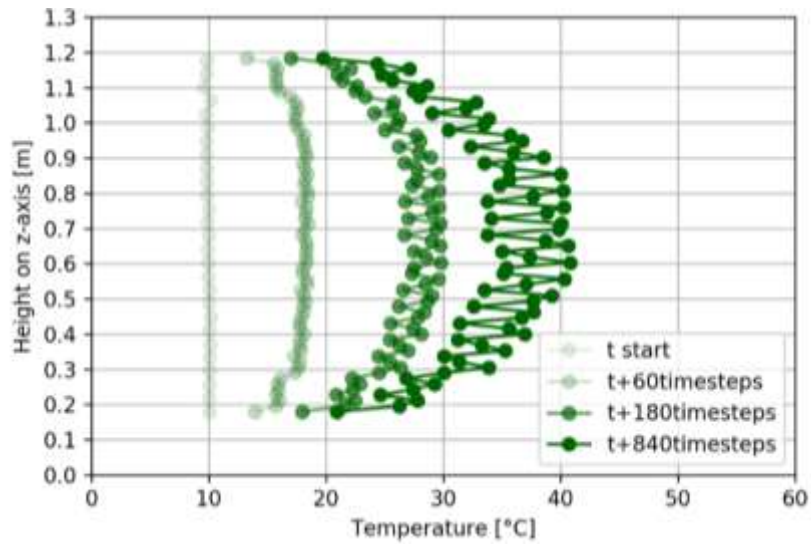


Figure 53: Fibreoptics Sensorpoint height over temperature @t+60, t+180 and t+840 timesteps (timestep-size = 1000s)

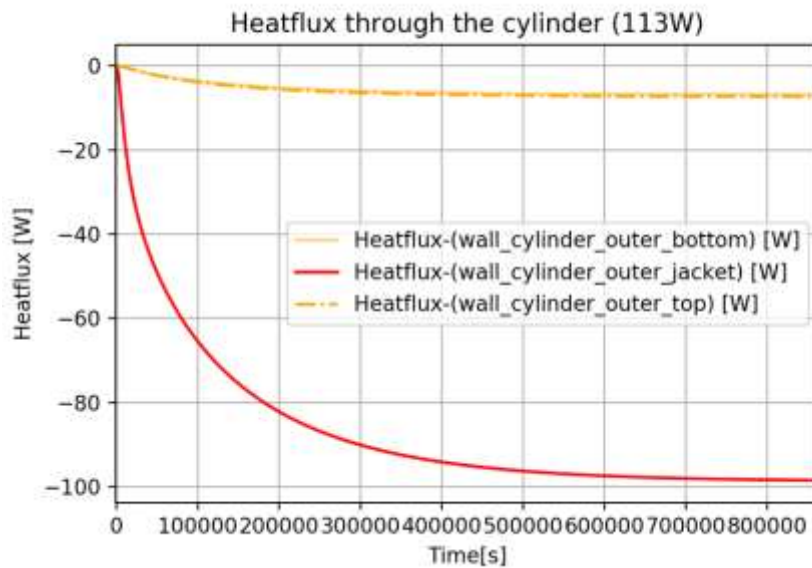


Figure 54: Negative heatflux through the cylinder walls over time

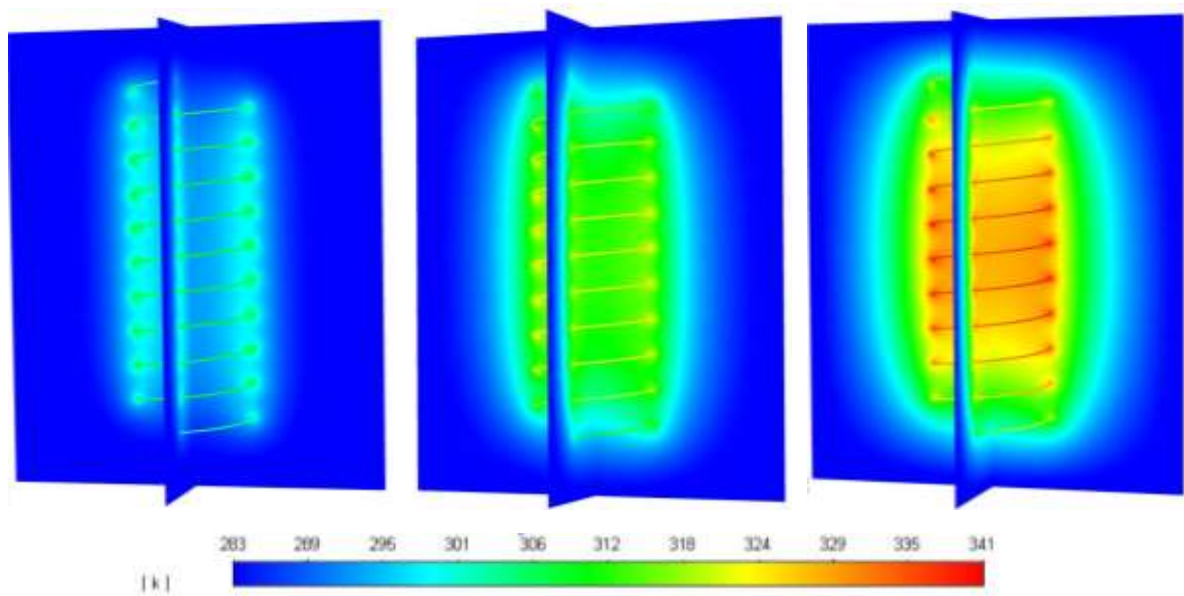


Figure 55: Contour plot @  $t+60$ , @  $t+180$  and @  $t+840$  timesteps (timestep-size = 1000s)

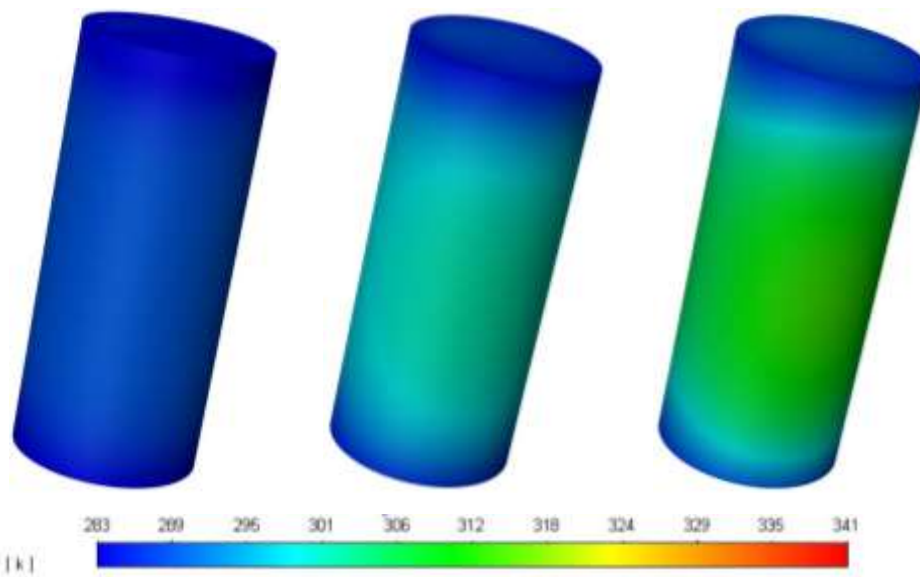


Figure 56: Contour plot of the cylinder\_outer\_jacket @  $t+60$ , @  $t+180$  and @  $t+840$  timesteps (timestep-size = 1000s)

## 11 Discussion and Results

In this chapter, results of this work are outlined and discussed. While parts of this work deal with the question how a sufficiently accurate simulation model can look like under the aspect of resource efficiency, others deal with the influence of different simulation parameters. It is important to understand, which soil properties ( $\lambda$ ,  $\rho$ ,  $c_p$ ) and further model parameters affect the temperature field in which way. As first comparisons of experiment and simulation (*chapter 8*) showed clear deviations of the temperature field ( $\frac{T_{exp}}{T_{sim}} = 2.1$ ), the origin had to be identified. The following can be presented:

The variation of the time-step size showed, that the time-step can be increased to a size of  $t = 1000s$ . Thus, calculation effort could be reduced significantly. Results are shown in *chapter 9.1*.

In a comparison of the 3D helix model and the 2D cylinder model, the 3D model shows higher temperature levels (especially in the near field around the heating helix) compared to levels of the 2D model. As the spiral pipe sections of the GHE interfere in z-direction (3D model), possible reason for this phenomenon could be seen in an early thermal saturation along the z-axis of the box. This saturation could have effects onto heat exchange, resulting in higher temperatures  $T$ . Further research work could be considered. In a comparison of the 2D cylinder model and the 1D rod model, both models show similar thermal behaviour regarding a variation of the thermal properties ( $\lambda$ ,  $\rho$ ,  $c_p$ ).

If talking about the BCs, varying the heat transfer coefficient  $\alpha$  showed, that the difference between simulation and experiment is not explainable by sole influence of forced convection of the cooling fan. The higher the heat transfer coefficient  $\alpha$  gets, the “harder” BCs get. “Hard” boundary conditions result in a steady state that is reached faster. Regarding the BCs, *Figure 29* and *Figure 53* show, that temperature-distribution  $T$  along the outer fibreoptics cable significantly “jump”. This could be explained by the cubic form of the box. Further improvement in terms of constructing the experimental test site could consider symmetry of pipe shapes for example to eliminate that factor.

Additionally *Figure 54* shows, that the heat flow through the cylinder wall flattens exponentially. It can be recognized, that the sum of power of the individual surfaces (bottom, top, jacket) result in the total power input of 113W as soon as thermal saturation (steady state) is reached. Energy that is injected into the system within a closed surface must also “leave” the system, as soon as talking about thermal saturation. This physical fact is mathematically formulated in Fourier’s heat conduction equation.

In terms of the mismatch between temperature levels of simulation and experiment it can be said, that the product of the material's density  $\rho$  and the specific heat capacity  $c_p$  provide information about the transient part of the differential equation only, while  $\lambda$  provides information about the steady-state solution. Low thermal conductivities  $\lambda$  lead to higher temperatures in steady state. This fact leads to the assumption of two possible set screws to adjust temperature levels of the simulation to experimental results:

- The Heat/Power Source [W]
- The value of the thermal conductivity  $\lambda$  [ $\text{W m}^{-1} \text{K}^{-1}$ ]

A variation of the power input showed, that simulation and experiment match to a certain degree, as soon as power is increased to  $P=280\text{W}$ . Results are shown in *Figure42 & Table3*. Further research work performed at AIT finally showed, that the disagreement of simulation and experiment truly had their origin in a wrong power measurement system on the experimental site. An SCR thyristor controller with phase angle control was installed in place of the old one. Temperature values in further simulations matched to experimental ones in a satisfying way. Results are shown in *Figure43*. Thus, the findings of this work were an important input to make further progress with the research work of earth baskets.

## 12 Outlook

As vertical spiral heat exchangers show high efficiency rates [15] and less sensitivity regarding ground temperature fluctuations compared to other configurations [13], literature is broadly in agreement, that vertical spiral GHE have high potential to be part of future heating systems. Furthermore heat pump systems in general are recognized to be a very exergy efficient way to convert renewable electricity into heat. If talking about the geometry configuration of future spiral GHEs, optimal pitch length is in between a maximum, where thermal performance converges, and a minimum pitch length, where thermal interference is dominant and limiting the performance. [10]

In order to get important insights into tendencies regarding the heat flows at different pitch heights and spiral diameters, an additional simulation series was carried out. This simulation series should be seen as an incentive for further research work to find optimal geometry parameters. Additionally *Figure59 & Figure61* should help to cultivate a scientific intercultural discourse to gain further understanding of the physical principles. Hopefully further work will (among others) increase market acceptance of GHEX heating systems to help finding a renewable way of heat supply for domestic applications.

## 12.1 Diameter Variation

The spiral diameter of the heating cable is reduced or increased by  $\pm 25\%$ , starting from a diameter of 350mm. The loop pitch is hold at constant value of  $p=100\text{mm}$ . This leads to following simulation parameters:

- Simulation 1:  $p= 100\text{mm}$ ,  $d= 280\text{mm}$ ,  $P= 113\text{W}$
- Simulation 2:  $p= 100\text{mm}$ ,  $d= 350\text{mm}$ ,  $P= 113\text{W}$
- Simulation 3:  $p= 100\text{mm}$ ,  $d= 437,5\text{mm}$ ,  $P= 113\text{W}$

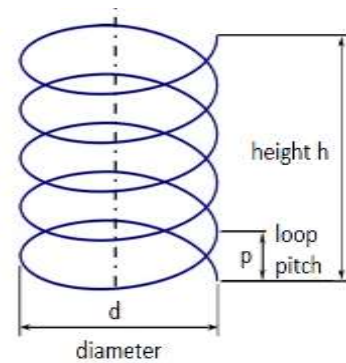


Figure 57: Parameters of the helix [19]

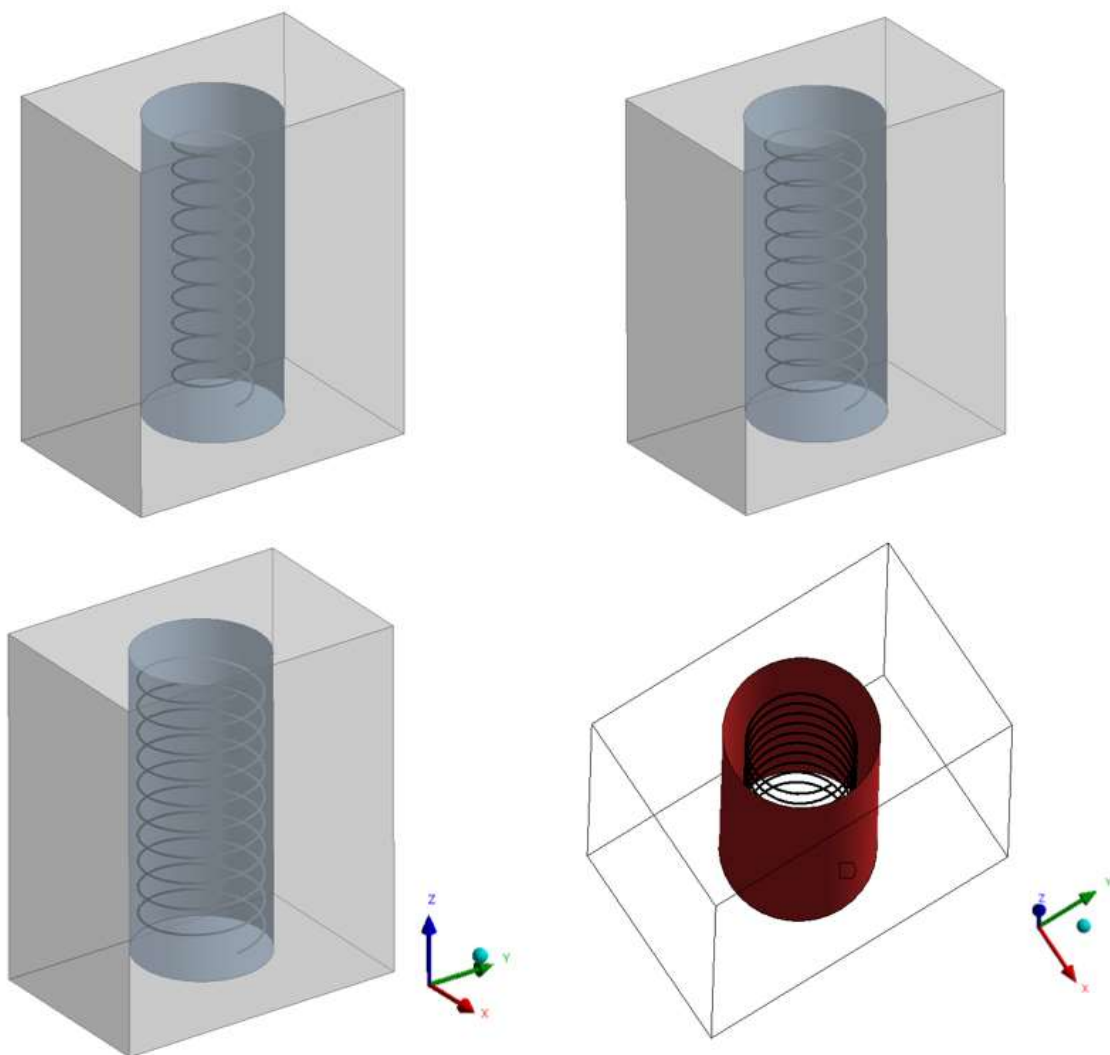


Figure 58: Loop-diameter = 280mm (topleft); Loop-diameter = 350mm (topright); Loop-diameter = 437,5mm (bottom-left); Jacket of the cylinder (bottom-right)

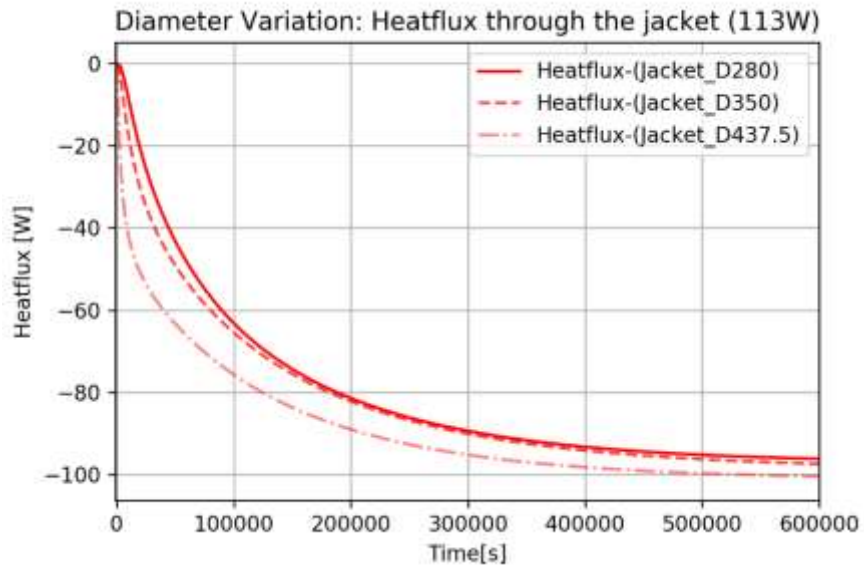


Figure 59: Heatflux through the jacket with varying diameter of the loop

## 12.2 Pitch Variation

In this simulation series, the spiral pitch length of the heating cable is reduced or increased by  $\pm 25\%$ , starting from a loop pitch of 100mm. The loop pitch is hold at constant value of  $p=100\text{mm}$ . This leads to following simulation parameters:

- Simulation1:  $p = 80\text{mm}$ ,  $d=280\text{mm}$
- Simulation2:  $p = 100\text{mm}$ ,  $d=280\text{mm}$
- Simulation3:  $p= 125\text{mm}$ ,  $d=280\text{mm}$

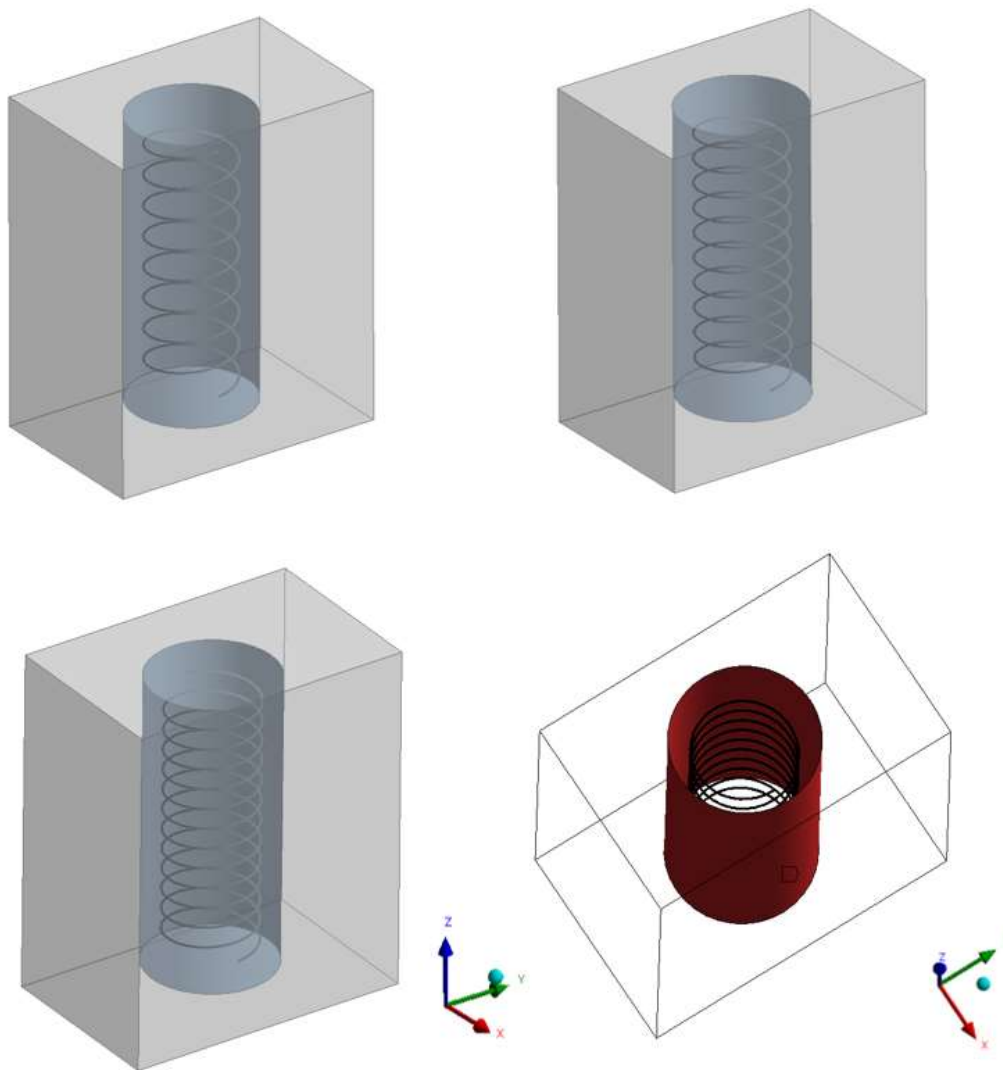


Figure 60: Loop-pitch = 125mm (topleft); Loop-pitch = 100mm (topright); Loop-pitch = 80mm (bottom-left); Jacket of the cylinder (bottom-right)

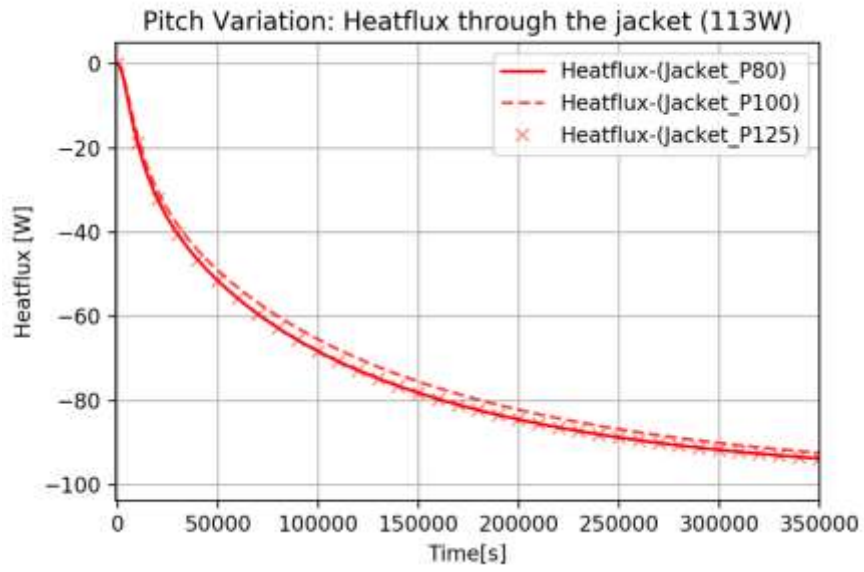


Figure 61: Heatflux through the jacket with varying pitch of the loop



## 13 Appendix

### 13.1 Material Properties

Attached the results of the laboratory characterization of dry sand with help of the standardized HFM measurement method. Uncertainty  $u$  of the measured properties is calculated according to equation ( 54 ). [21]

$$a = \frac{\lambda}{\rho * c} \quad (53)$$

$$u^2(a) = \frac{u^2(\lambda) - (a * \rho)^2 * u^2(c_p) - (a * c_p)^2 u^2(\rho)}{(c_p * \rho)^2} \quad (54)$$

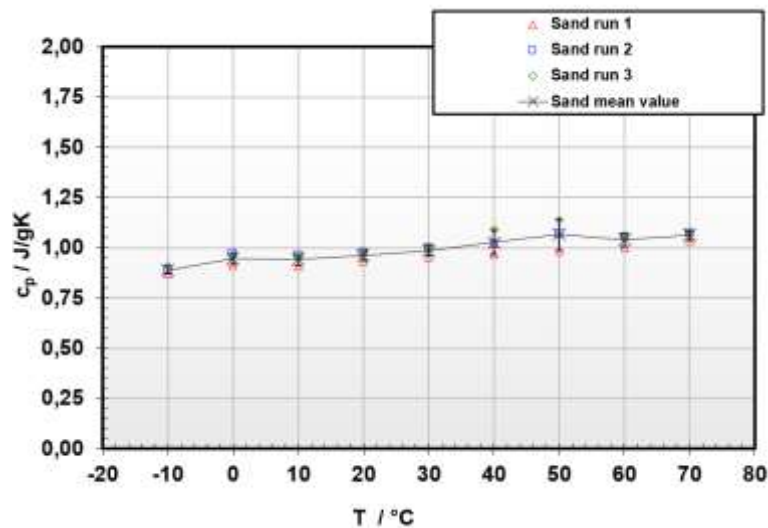


Figure 62: specific heat capacity of dry sand over temperature T [21]

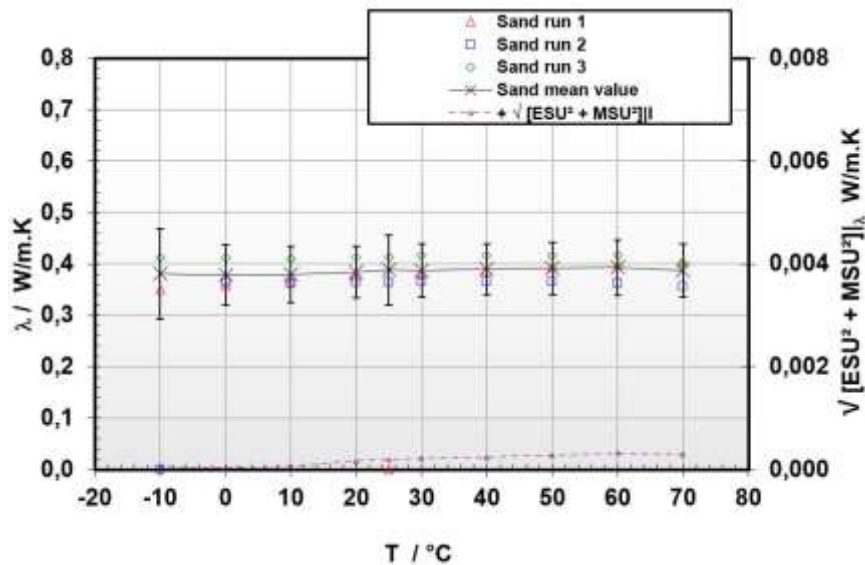


Figure 63: thermal conductivity of dry sand over temperature T [21]

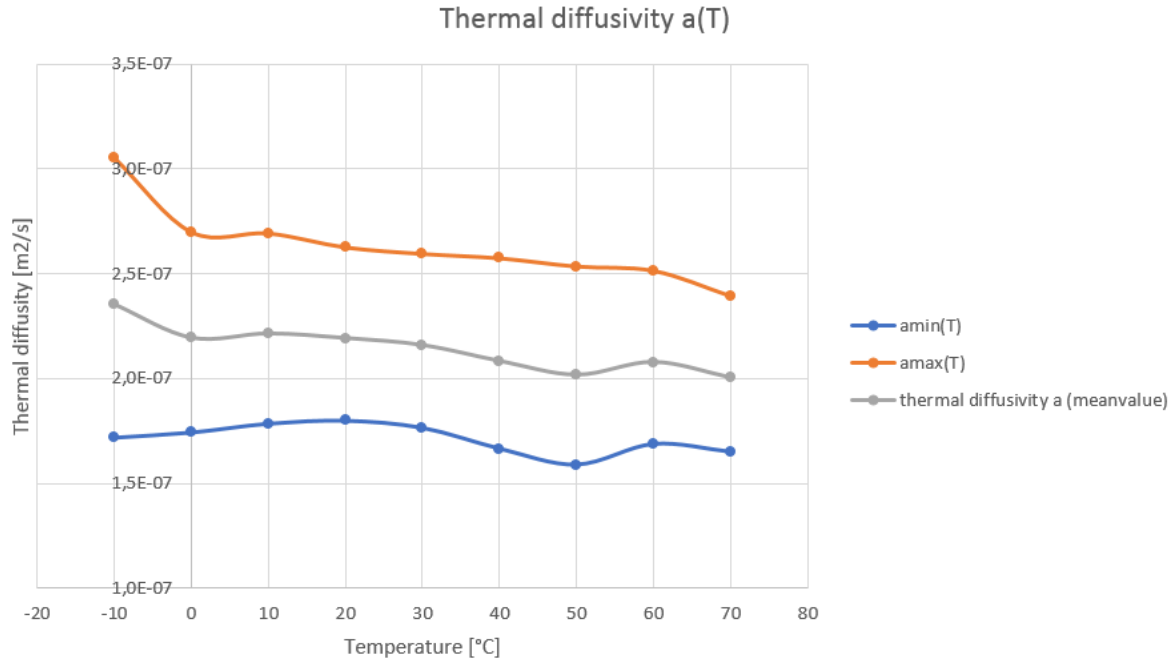


Figure 65: Uncertainty limits of the thermal diffusivity  $a$

## 13.2 Sensorpoint data

Construction of the sensorpoint helix				
Parameter	Parameter declaration	Inner basket [mm]	Middle basket [mm]	Outer basket [mm]
Diameter of the heating coil basket	dcb	200,00	350,00	500,00
Radius of the heating coil basket	rcb	100,00	175,00	250,00
Diameter fibre optics cable	dfo	7,30	7,30	7,30
Radius fibre optics cable	rfo	3,65	3,65	3,65
Radius of fibre optics coil basket	rfocb	103,65	178,65	253,65
Offset in z-direction	c	180,00	180,00	180,00
Slopedistance	h	100,00	100,00	100,00
Starting parameter	t	0,00	0,00	0,00
Incremental step size	$\Delta t$	0,38	0,22	0,16

Table 4: Parameters of the sensorpoint helix

Sensorpoint-coordinates	X [m]	Y [m]	Z [m]
Inner i13	0.103460	-0.006260	0.679040
Middle m23	0.128270	0.124350	0.692250
Outer o33	0.112970	0.227100	0.697650

Table 5: Location of the sensorpoints i13, m23, o33 in the model domain

## References

1. Grant Agreement-792210-GeoFit
2. Javadi H, Mousavi Ajarostaghi SS, Rosen MA et al. (2019) Performance of ground heat exchangers: A comprehensive review of recent advances. *Energy* 178:207–233. <https://doi.org/10.1016/j.energy.2019.04.094>
3. Al-Khoury R. (2011) Computational modeling of shallow geothermal systems.
4. Burkhard Sanner (2003) Current status of ground source heat pumps in Europe. *Inst. of Applied Geosciences*
5. Yang W, Lu P, Chen Y (2016) Laboratory investigations of the thermal performance of an energy pile with spiral coil ground heat exchanger. *Energy and Buildings* 128:491–502. <https://doi.org/10.1016/j.enbuild.2016.07.012>
6. DI Constantin Julian Dörr (2020) CFD Analysis of Ground Source Heat Exchangers. Master's thesis
7. Jeon J-S, Lee S-R, Kim M-J et al. (2018) Suggestion of a Scale Factor to Design Spiral-Coil-Type Horizontal Ground Heat Exchangers. *Energies* 11:2736. <https://doi.org/10.3390/en11102736>
8. Tu S, Zhang X, Zhou X (2017) A revised thermal resistance and capacity model for the ground heat exchanger under freezing soil conditions and thermal performance analysis. *Procedia Engineering* 205:19–26. <https://doi.org/10.1016/j.pro-eng.2017.09.929>
9. Bauer M, Freeden W, Jacobi H et al. (2018) *Handbuch Oberflächennahe Geothermie*. Springer Berlin Heidelberg, Berlin, Heidelberg
10. Kim M-J, Lee S-R, Yoon S et al. (2018) Evaluation of geometric factors influencing thermal performance of horizontal spiral-coil ground heat exchangers. *Applied Thermal Engineering* 144:788–796. <https://doi.org/10.1016/j.applthermaleng.2018.08.084>
11. Congedo PM, Colangelo G, Starace G (2012) CFD simulations of horizontal ground heat exchangers: A comparison among different configurations. *Applied Thermal Engineering* 33-34:24–32. <https://doi.org/10.1016/j.applthermaleng.2011.09.005>
12. Sáez Blázquez C, Farfán Martín A, Martín Nieto I et al. (2017) Efficiency Analysis of the Main Components of a Vertical Closed-Loop System in a Borehole Heat Exchanger. *Energies* 10:201. <https://doi.org/10.3390/en10020201>
13. Chong CSA, Gan G, Verhoef A et al. (2013) Simulation of thermal performance of horizontal slinky-loop heat exchangers for ground source heat pumps. *Applied Energy* 104:603–610. <https://doi.org/10.1016/j.apenergy.2012.11.069>
14. Piechowski M (1998) Heat and mass transfer model of a ground heat exchanger: validation and sensitivity analysis. *Int J Energy Res* 22:965–979. [https://doi.org/10.1002/\(SICI\)1099-114X\(199809\)22:11<965:AID-ER421>3.0.CO;2-G](https://doi.org/10.1002/(SICI)1099-114X(199809)22:11<965:AID-ER421>3.0.CO;2-G)

15. Bezyan B, Porkhial S, Mehrizi AA (2015) 3-D simulation of heat transfer rate in geothermal pile-foundation heat exchangers with spiral pipe configuration. *Applied Thermal Engineering* 87:655–668. <https://doi.org/10.1016/j.applthermaleng.2015.05.051>
16. Univ. Prof. Dipl. -Ing. Dr. techn. Harald Raupenstrauch (2013) *Vorlesungsunterlagen Wärmeübertragung*, 3. Auflage
17. Schmidt A (2019) *Technical Thermodynamics for Engineers*. Springer International Publishing, Cham
18. Böckh P, Wetzel T (2017) *Wärmeübertragung*. Springer Berlin Heidelberg, Berlin, Heidelberg
19. Stephan\_Kling (2020) *Experimental Characterization of Helix- Type Ground Source heat Exchanger Configurations for Developing a Standardized Design Tool*. Master's Thesis
20. Nowak, T., Westring, P., (2019). *European Heat Pump Market and Statistics Report*
21. AIT Austrian Institute of Technology, 2020. Geofit research project
22. World Wide Web. March 2021. URL:  
<https://geofit-project.eu/project/objectives/>